International Journal of Numerical Methods in Engineering (in review)

Two-Level Multiscale Enrichment Methodology for Modeling of Heterogeneous Plates

Caglar Oskay*

Department of Civil and Environmental Engineering
Vanderbilt University
Nashville, TN, 37235

Abstract

A new two-level multiscale enrichment methodology for analysis of heterogeneous plates is presented. The enrichments are applied in the displacement and strain levels: the displacement field of a Reissner-Mindlin plate is enriched using the multiscale enrichment functions based on the partition of unity principle; the strain field is enriched using the mathematical homogenization theory. The proposed methodology is implemented for linear and failure analysis of brittle heterogeneous plates. The eigendeformation-based model reduction approach is employed to efficiently evaluate the nonlinear processes in case of failure. The capabilities of the proposed methodology are verified against direct three-dimensional finite element models with full resolution of the microstructure.

Keywords: multiscale; homogenization; partition of unity; composite plates; model reduction

1 Introduction

Modeling and simulation of heterogeneous and composite systems has been an important research subject in the past few decades. With the advent of multiscale modeling and simulation technology, significant strides have been made in modeling and understanding of complex, nonlinear phenomena associated with the mechanical response of these materials. While, many of the complex heterogeneous and composite systems are manufactured and used in the form of plates and shells, most of the recent development has focused on the modeling of solid heterogeneous systems. In this manuscript, we focus on the multiscale modeling of linear and nonlinear heterogeneous plates. A novel two-level multiscale enrichment methodology is proposed to model the response of heterogeneous systems in the context of plate theory. The proposed approach has its roots in the mathematical homogenization theory and multiscale enrichment by partition of unity methods, but it extends these methods to the analysis of heterogeneous plate structures.

*VU Station B#351831, 2301 Vanderbilt Place, Nashville, TN 37235. Email: caglar.oskay@vanderbilt.edu

Mathematical homogenization theory (MHT) is the most mathematically rigorous tool for analysis of heterogeneous materials and structures. Since its inception with the seminal works of Babuska [1], Bensoussan [2], Sanchez-Palencia [3], Suquet [4] and others, it has been popular in the academic world and is slowly taking root in the industry largely due to efforts to incorporate MHT based computational methods into commercially available computer codes [5]. The MHT results in the enrichment of the macroscopic strain fields using influence functions, which represent the effects of microscopic deformation modes. A number of restrictions in the theory limit the applicability and faster acceptance of MHT based modeling methods: The first is the scale separation assumption. The theory separates the microscopic and macroscopic scales through asymptotic analysis with the help of periodicity condition. The theory is valid when the characteristic scale ratio (defined as the ratio between the characteristic lengths of the microscopic and macroscopic scales) is very small, and the macroscopic response fields are smooth. Second, the MHT based computational methods are typically cumbersome for nonlinear analysis of large-scale structures. This is because integration of macroscopic stresses requires evaluation of an RVE problem at every macroscopic integration point at each iteration of each increment - a tremendous computational burden.

One modeling approach for evaluating heterogeneous systems without scale separations is by hierarchical decomposition of the displacement field into macroscopic and microscopic counterparts. The microscopic displacement field is treated as enrichment to the macroscopic fields, which are typically discretized using the standard finite element shape functions. The enrichment fields are non-standard basis functions embodying the response characteristics of the microscopic heterogeneities. Variational multiscale methods formalized by Hughes [6] and partition of unity method formalized by Babuska and Melenk [7] provide rigorous frameworks for enrichment of the macroscopic fields with local basis functions with compact support. Yu and coworkers applied the displacement enrichment strategy to model the mechanical and functional response of thin composite plates [8, 9, 10]. In this formulation, 3-D warping functions are employed to enrich the Reissner-Mindlin theory. Additional methods with similar characteristics have also been proposed in the context of heterogeneous material modeling (see, e.g., [11]). More recently, Fish and Yuan [12, 13] developed a multiscale enrichment methodology based on the partition of unity principle to characterize the response of linear and nonlinear heterogeneous materials. In this method, the macroscopic standard finite element basis is enriched using the influence functions of the classical mathematical homogenization method. This method was shown to be effective in capturing the response even in the presence of high stress and strain gradient zones present around a crack tip.

Two approaches have been proposed to circumvent the second restriction of MHT. The first one is a brute force approach: the micro-level RVE computations are distributed to massively parallel compute nodes [14]. Since the RVE evaluations at a given iteration can be conducted independently, significant cost reduction is possible by this approach. The second approach is the reduction of the microscopic model order by replacing the original RVE problem with a lower order approximation. Voronoi cell method [15], Fourier transform [16], spectral [17], R3M [18] and transformation field analysis [19, 20, 21, 22] based methods, among others, have been recently proposed to evaluate the nonlinear response of heterogeneous materials. Eigendeformation-based model reduction methodology, recently proposed by Oskay and Fish [23] provides an efficient and effective means for reducing the model order and analysis of nonlinear heterogeneous systems.

A majority of the current state-of-the-art model reduction approaches are concerned with reducing the size of the RVE problem only. Attempts to reduce the order of the macroscopic problem, on the other hand, have been relatively rare. Analysis of plate and shell structures call for an alternative approach to model reduction by exploiting the size disparity between thickness and the characteristic length of the macroscale, in addition to the characteristic scale ratio. Asymptotic analysis with two characteristic scale ratios have been proposed to analyze the response of plates, shells and other structural components including rods and beams [24, 25, 26, 27, 28]. Mathematical homogenization of thin heterogeneous plates typically leads to Kirchhoff-type models. The properties of the resulting homogenized plates depend on the ratio between the two characteristic length ratios [29]. More recently, a combined micro-macro model reduction methodology has been proposed by Oskay and Pal [30] for failure analysis of thin heterogeneous plates. In this approach, the eigendeformation-based model reduction methodology is applied in the context of nonlinear mathematical homogenization of thin plates. The applicability of many MHT-based heterogeneous plate models is restricted to the analysis of very thin domains, where the Kirchhoff assumptions are valid in the macroscale.

In this manuscript, a two-level enrichment methodology is presented for analysis of heterogeneous structures. A higher order plate theory is derived by enriching a Reissner-Mindlin plate using first and second order multiscale enrichment functions. The enrichment functions, which are obtained through MHT, are introduced by employing the partition of unity method. Linear and nonlinear problems are analyzed. In the nonlinear case, the formulation for failure of structures composed of brittle heterogeneous materials is given. The failure within the microstructure is idealized by considering degradation of the material properties of the micro-constituents (e.g., fiber, matrix) through microcracking. The eigendeformation-based model reduction methodology is employed to increase the computational efficiency of the model. The proposed failure model proves advantageous compared to current modeling approaches because (1) the microscopic kinematics is captured accurately with a few additional basis functions using the multiscale enrichment methodology, and (2) plates with arbitrary microstructures can be modeled, extending beyond the traditional laminated composite paradigm including 3-D and complex composite architectures. The proposed work is novel in the following respects: (a) The multiscale enrichment methodology originally proposed in [12] for 3-D solid continua is applied to the structural theory for the first time; (b) a novel fast integration scheme is introduced to efficiently evaluate the macroscale element matrix computations without recourse to computationally costly homogenization-like integration scheme, and; (c) the multiscale enrichment and eigendeformation-based model reduction methodologies have been seamlessly integrated and associated computational algorithms are provided.

This manuscript is organized as follows: Section 2 describes the setting of the problem and assumptions regarding the domain of the heterogeneous body. In Section 3, we state the multiscale enrichment functions for analysis of linear heterogeneous plates and discuss their characteristics. A novel integration scheme is presented for multiscale enrichment methodology. The capabilities of the linear enrichment functions are verified against direct 3-D finite element analysis of plates with full resolution of the microscopic details and the thickness direction. In Section 4, the failure model and the setting for the nonlinear plate problem is described. A nonlinear enrichment methodology based on eigendeformation-based reduced order modeling approach is presented. Details of the numerical implementation of the proposed model in a commercial finite element code and the verification against 3-D finite element simulations are provided. Section 5 concludes the manuscript by discussion of the results and future research directions.

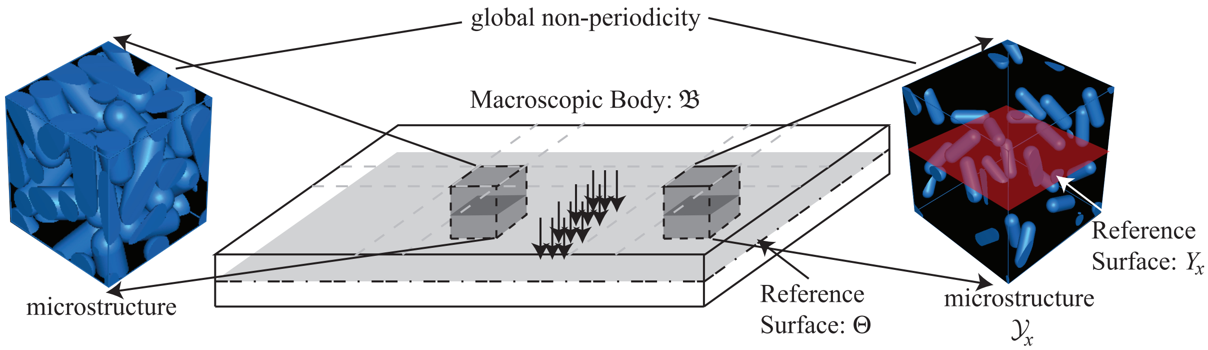

Figure 1: The domain of the heterogeneous plate composed of globally non-periodic microstructures of arbitrary complexity.

2 Problem Setting

Consider a heterogeneous plate with domain, $\mathcal{B}$, as shown in Fig. 1:

$$\mathcal{B} := \left\{ \mathbf{x} \,|\, \mathbf{x} = (x, z),\; x = \{x_1,\, x_2\} \in \Theta,\; -\frac{1}{2} t\,(x) \leq z \leq \frac{1}{2} t\,(x) \right\} \tag{1}$$

where, $\Theta \in \mathbb{R}^2$ is the reference surface parameterized by the Cartesian coordinate vector, x; z-axis denotes thickness direction perpendicular to Θ; $\mathbf{x} = \{x_1,\, x_2,\, z\}$ the three-dimensional position vector, and; t define the top and bottom boundaries of the body. The thickness of the plate is considered to be small compared to the characteristic deformation wavelength of the structure. The heterogeneous plate domain, $\mathcal{B}$, is composed of non-overlapping representative volume elements (RVEs) within the boundaries of the structure:

$$\mathcal{B} = \bigcup_{\text{all RVEs}} \mathcal{Y}_x \tag{2}$$

The domain of an RVE is defined as:

$$\mathcal{Y}_x := \left\{ \mathbf{x} \,|\, \mathbf{x} = (x, z),\; x = \{x_1,\, x_2\} \in Y_x \subset \Theta,\; -\frac{1}{2} t\,(x) \leq z \leq \frac{1}{2} t\,(x) \right\} \tag{3}$$

in which $Y_x \in \mathbb{R}^2$ is the reference surface in the RVE. We assume *local* periodicity of the RVE: the microstructure is allowed to be different along the length of the plate, yet it is taken to be repetitive at the locality of an RVE. While this condition is not necessary for the enrichment approach, it significantly simplifies the element level computations. The boundaries of an RVE are defined as:

$$\partial \mathcal{Y}_x^z = \left\{ \mathbf{x} \,|\, x \in Y_x,\; z = \pm \frac{1}{2} t(x) \right\} \tag{4}$$

$$\partial \mathcal{Y}_x^{\text{per}} = \left\{ \mathbf{x} \,|\, x \in \partial Y_x,\; -\frac{1}{2} t(x) < z < \frac{1}{2} t(x) \right\} \tag{5}$$

in which, ∂Y_x denotes the boundaries of the RVE reference surface.

In what follows, Greek subscripts denote 1 and 2, unless otherwise indicated, while lower-case Roman indices denote 1, 2 and 3, with $x_3 = z$.

3 Multiscale Enrichment of Linear Heterogeneous Plates

In this section, the two-level multiscale enrichment methodology is introduced in the context of linear heterogeneous plate problems. The formulation of the enrichment methodology and the properties of the linear enrichment functions, computational aspects, and numerical verification of the methodology are described.

3.1 Formulation

The starting point for the enrichment formulation is the three-dimensional governing equations of a heterogenous plate illustrated in Fig. 1. In this section, each microconstituent is assumed to be linear-elastic with perfect bonding along the interfaces. The displacement field is expressed in the following form:

$$u_i(\mathbf{x}) = u_i^0(x) - z\delta_{i\alpha}\theta_\alpha(x) + H_{iA}(\mathbf{x})\,\eta_A(x) \tag{6}$$

in which, u_i^0 denotes the displacement components on the reference surface, Θ; θ_α the rotations; H_{iA} the displacement enrichment functions, and; η_A smooth functions introduced to satisfy the partition of unity property of the enrichment. Plate theories with varying degree of complexity are obtained by choosing appropriate number of (typically) polynomial forms for H_{iA} (see e.g., Refs [31]) along with the kinetic conditions to satisfy displacement and stress continuity within the microstructure. Appropriate selection of the enrichment functions is therefore critical to efficient and accurate representation of the deformation fields within the structure. In this manuscript, we employ the influence functions of the classical mathematical homogenization theory as the enrichment functions. The influence functions are the solutions to the first and second order linear influence function problems defined on the RVE domain:

IFP1: First Order Influence Function Problem:

$$\left[L_{ijmn}\left(H^1_{(m,n)kl} + I_{mnkl}\right)\right]_{,j} = 0 \quad \text{on } \mathcal{Y}_x \tag{7a}$$

$$H^1_{ikl}\ \mathbf{x}\text{-periodic on } \partial\mathcal{Y}_x^{\text{per}};\quad H^1_{ikl}\ x\text{-periodic on } \partial\mathcal{Y}_x^{\text{z}} \tag{7b}$$

$$e_i^z L_{ijmn}\left(H^1_{(m,n)kl} + I_{mnkl}\right) n_j = 0 \text{ on } \partial\mathcal{Y}_x^{\text{z}} \tag{7c}$$

IFP2: Second Order Influence Function Problem:

$$\left[L_{ijmn}\left(H^2_{(m,n)kl} - zI_{mnkl}\right)\right]_{,j} = 0 \quad \text{on } \mathcal{Y}_x \tag{8a}$$

$$H^2_{ikl}\ \mathbf{x}\text{-periodic on } \partial\mathcal{Y}_x^{\text{per}};\quad H^2_{ikl}\ x\text{-periodic on } \partial\mathcal{Y}_x^{\text{z}} \tag{8b}$$

$$e_i^z L_{ijmn}\left(H^2_{(m,n)kl} - zI_{mnkl}\right) n_j = 0 \text{ on } \partial\mathcal{Y}_x^{\text{z}} \tag{8c}$$

where, L_{ijkl} is the tensor of elastic moduli, which varies within the RVE due to material heterogeneity; $\mathbf{e}^z$ denotes the unit vector along the z direction, and; n_j the normal vector. The boundary conditions provided in IFP1 and IFP2 are augmented by restricting the rigid body modes. $\mathbf{x}$-periodicity denotes periodicity in all three directions, while x-periodicity denotes periodicity along the directions defining the reference surface. The boundary conditions constitute a mixture of traction and periodic boundary conditions. This particular choice ensures that the homogenized stiffness of the RVE reduces to the plane-stress condition in the

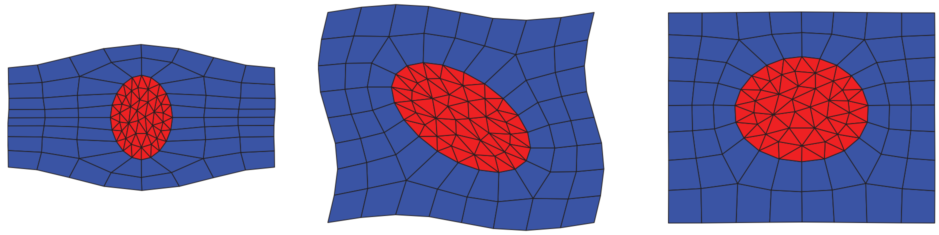

(a) (b) (c)

Figure 2: The components of the elastic influence functions for a 2-D matrix with circular inclusion: (a) H^1_{i11}; (b) H^1_{i12}; (c) H^2_{i11}.

homogeneous limit. This condition is illustrated in Appendix A. The enrichment functions for the three-dimensional case are taken as $H_{iA} \leftarrow \left\{ H^1_{i\alpha\beta},\, H^2_{i\alpha\beta}, H^1_{i\alpha 3} \right\}$. The components of a two-dimensional two-phase composite with constant Poisson's ratio and matrix/inclusion stiffness ratio of 0.3 are shown in Fig. 2. Three enrichment functions are introduced in 2-D: $H_{iA} \leftarrow \left\{ H^1_{i11},\, H^2_{i11}, H^1_{i12} \right\}$. The influence functions have the following characteristics:

1. The influence functions are unique with the provided boundary conditions. Traction homogeneity is assumed normal to the reference surface along with the periodicity in the remaining boundaries and directions. The proof follows from the standard analysis techniques used in the classical homogenization theory [2].
2. The plate is allowed to deform along the thickness direction as illustrated in Fig. 2a.
3. H_{iA} introduces higher order deformation modes as illustrated in Fig. 2.

The accuracy and convergence properties of the enrichment functions are assessed numerically in this manuscript. Mathematical analysis of the enrichment functions proposed herein will be conducted in a future publication.

The second enrichment is in the strain level. The strain field is enriched by employing the first and second order influence functions:

$$\epsilon_{ij}\left(\mathbf{x}\right) = A^1_{ij\alpha\beta}\left(\mathbf{x}\right) e_{\alpha\beta}\left(x\right) + A^2_{ij\alpha\beta}\left(\mathbf{x}\right) \kappa_{\alpha\beta}\left(x\right) + A^3_{ij\alpha}\left(\mathbf{x}\right) \gamma_\alpha\left(x\right) + \hat{\epsilon}_{ij}\left(\mathbf{x}\right) \tag{9}$$

in which, $e_{\alpha\beta} = u^0_{(\alpha,\beta)}$ is the macroscopic in-plane strain; $\kappa_{\alpha\beta} = \theta_{(\alpha,\beta)}$ the macroscopic curvature; $\gamma_\alpha = u^0_{3,\alpha} - \theta_\alpha$ the macroscopic transverse shear, and $\hat{\epsilon}_{ij}$ is the strain tensor due to the displacement enrichment functions. The formulation is restricted to the small strains. The strain concentration tensors are expressed in terms of the influence functions:

$$A^1_{ij\alpha\beta} = I_{ij\alpha\beta} + G^1_{ij\alpha\beta}; \quad A^2_{ij\alpha\beta} = -zI_{ij\alpha\beta} + G^2_{ij\alpha\beta}; \quad A^3_{ij\alpha} = I_{ij\alpha 3} + G^1_{ij\alpha 3}; \tag{10}$$

where, $G^p_{ijkl} = H^p_{(i,j)kl}$, $p = 1, 2$ are the polarization tensors.

3.2 Classical Multiscale Enrichment based on Partition of Unity

The macroscopic displacement components u^0_i, θ_α, and η_A are discretized based on the standard 2-D finite element shape functions, $N_a\left(x\right)$ defined on the reference surface Θ:

$$u^0_i\left(x\right) = N_a\left(x\right) c^0_{ia}; \quad \theta_\alpha\left(x\right) = N_a\left(x\right)\theta_{\alpha a}; \quad \eta_A\left(x\right) = N_a\left(x\right)\eta_{Aa}; \quad a = 1, 2, \ldots, n_{node} \tag{11}$$

where, n_{node} is the number of nodes along the reference surface, Θ. The discretization of all the macroscopic displacement components using the same shape functions is not a necessary condition of the formulation. Similar formulations may be achieved by employing separate shape functions for each component. We use a standard Galerkin formulation to discretize the macroscopic domain of the structure. In what follows, we concentrate on the numerical formulation at the element level. The global matrices are established using standard assembly procedures [32].

Within a finite element, the displacement field is expressed in the matrix form as:

$$\mathbf{u}(\mathbf{x},t) = \boldsymbol{\mathcal{N}}(\mathbf{x})\,\mathbf{c} \tag{12}$$

in which, $\boldsymbol{\mathcal{N}} = \{\boldsymbol{\mathcal{N}}_1, \boldsymbol{\mathcal{N}}_2, \ldots, \boldsymbol{\mathcal{N}}_{n_{en}}\}$, and

$$\boldsymbol{\mathcal{N}}_a(\mathbf{x}) = \left[\begin{array}{ccccc|c} 1 & 0 & 0 & -z & 0 & \\ 0 & 1 & 0 & 0 & -z & \mathbf{H}_a(\mathbf{x}) \\ 0 & 0 & 1 & 0 & 0 & \end{array}\right] N_a(x) \tag{13}$$

in which, n_{en} denotes the number of nodes in a macroscopic finite element; N_a the shape function at node a; $\mathbf{c} = \left\{c^0_{ia},\, \theta_{\alpha a},\, \eta_{Aa}\right\}$ denotes the vector of nodal coefficients for standard and enrichment degrees of freedom. $\mathbf{H}_a$, are the enrichment functions associated with node a:

$$\mathbf{H}_a(\mathbf{x}) = \begin{bmatrix} H^1_{111} & H^1_{122} & H^1_{112} & H^2_{111} & H^2_{122} & H^2_{112} & H^1_{113} & H^1_{123} \\ H^1_{211} & H^1_{222} & H^1_{212} & H^2_{211} & H^2_{222} & H^2_{212} & H^1_{213} & H^1_{223} \\ H^1_{311} & H^1_{322} & H^1_{312} & H^2_{311} & H^2_{322} & H^2_{312} & H^1_{313} & H^1_{323} \end{bmatrix} N_a(x) \tag{14}$$

where $H^p_{ikl} = H^p_{ikl}(\mathbf{x})$; $p = 1, 2$.

The strain field for the proposed displacement field decomposition reads:

$$\boldsymbol{\epsilon}(\mathbf{x}) = \boldsymbol{\mathcal{B}}(\mathbf{x})\,\mathbf{c} \tag{15}$$

The components of the $\boldsymbol{\mathcal{B}} = \{\boldsymbol{\mathcal{B}}_1, \boldsymbol{\mathcal{B}}_2, \ldots, \boldsymbol{\mathcal{B}}_{n_{en}}\}$ are expressed as:

$$\boldsymbol{\mathcal{B}}_a(\mathbf{x}) = \left[\begin{array}{c|c} \mathbf{A}^1(\mathbf{x})\,\mathbf{B}^e_a + \mathbf{A}^2(\mathbf{x})\,\mathbf{B}^\kappa_a + \mathbf{A}^3(\mathbf{x})\,\mathbf{B}^\gamma_a & \hat{\mathbf{G}}_a(\mathbf{x}) \end{array}\right] \tag{16}$$

where,

$$\boldsymbol{\mathcal{B}}^e_a(x) = \begin{bmatrix} N_{a,x} & 0 & 0 & 0 & 0 \\ 0 & N_{a,y} & 0 & 0 & 0 \\ N_{a,y} & N_{a,x} & 0 & 0 & 0 \end{bmatrix} \tag{17}$$

$$\boldsymbol{\mathcal{B}}^\kappa_a(x) = \begin{bmatrix} 0 & 0 & 0 & N_{a,x} & 0 \\ 0 & 0 & 0 & 0 & N_{a,y} \\ 0 & 0 & 0 & N_{a,y} & N_{a,x} \end{bmatrix} \tag{18}$$

$$\boldsymbol{\mathcal{B}}^\gamma_a(x) = \begin{bmatrix} 0 & 0 & N_{a,x} & -N_a & 0 \\ 0 & 0 & N_{a,y} & 0 & -N_a \end{bmatrix} \tag{19}$$

Using the indicial notation, the components of $\hat{\mathbf{G}}_a$ are expressed as:

$$\left(\hat{G}^p_{ijkl}\right)_a = H^p_{(i,j)kl} N_a + H^p_{ikl} N_{a,j} + H^p_{jkl} N_{a,i} \tag{20}$$

and, $\mathbf{A}^1$, $\mathbf{A}^2$ and $\mathbf{A}^3$ are the strain concentration functions expressed in the matrix form.

3.2.1 Numerical Integration

The discrete system of equations obtained by the Galerkin formulation leads to an element stiffness tensor of the form:

$$\mathbf{K}^e = \int\limits_{A^e} \int\limits_{-t(x)}^{t(x)} \boldsymbol{\mathcal{B}}^T(\mathbf{x})\,\mathbf{L}(\mathbf{x})\,\boldsymbol{\mathcal{B}}(\mathbf{x})\,dAdz \tag{21}$$

Consider a scaling constant defined as a ratio between the size of the in-plane dimensions of the RVE and the macroscopic finite element ($\zeta = |Y|/|A^e|$). When $\zeta \ll 0$, a homogenization like integration (HLI) scheme is sufficient to numerically evaluate the element stiffness matrix. In the homogenization like integration scheme, the stiffness matrix is integrated over n_{int} RVEs placed at the integration points of the macroscopic element:

$$\mathbf{K}^e \cong \sum_{I=1}^{n_{int}} W_I J_I \left\langle \boldsymbol{\mathcal{B}}^T \mathbf{L} \boldsymbol{\mathcal{B}} \right\rangle \tag{22}$$

The HLI scheme asymptotically converges to the full integration of all RVEs within the finite element at the scale separation limit (as the scaling constant approaches zero) [12]. For larger values of the scaling constant, a full integration within the finite element is necessary.

3.3 HLI-Free Homogenization Operator for Multiscale Enrichment

The HLI and full integration schemes are computationally costly compared to classical strain-only enrichment because of the necessity of integration over RVE domains. In strain only enrichment schemes, the Hill-Mandel condition is typically employed, avoiding the integration over the microscopic scales. In higher order homogenization approaches, asymptotic or tailor series expansions are introduced to derive higher order micro-macro energy balance equations. In this section, a novel homogenization operator is introduced to avoid the numerical integration of the stiffness matrix and the force vector.

The energy equivalence between the micro- and macroscopic scales in the strain-only enrichment case ($\hat{\epsilon}_{ij} = 0$) yields:

$$\langle \sigma_{ij}\epsilon_{ij} \rangle = \langle \sigma_{\alpha\beta} \rangle e_{\alpha\beta} + \langle -z\sigma_{\alpha\beta} \rangle \kappa_{\alpha\beta} + \langle \sigma_{\alpha 3} \rangle \gamma_\alpha \tag{23}$$

in which, $\langle \sigma_{\alpha\beta} \rangle$, $\langle -z\sigma_{\alpha\beta} \rangle$ and $\langle \sigma_{\alpha 3} \rangle$ are the homogenized in plane force, moment and shear force resultants, respectively. This expression is in contrast with the Hill-Mandel condition for fully periodic RVEs: $\langle \sigma_{ij}\epsilon_{ij} \rangle = \langle \sigma_{ij} \rangle \langle \epsilon_{ij} \rangle$. The alternative expression for the micro-macro energy balance is because the RVE average of the enrichment functions does not necessarily vanish. This characteristic is demostrated by considering a uniform RVE in Appendix A. A partial derivation of Eq. 23 is provided in Appendix B. In the general two-level enrichment case ($\hat{\epsilon}_{ij} \neq 0$), the energy equivalence may be expressed as (see Appendix B):

$$\langle \sigma_{ij}\epsilon_{ij} \rangle = \bar{\sigma}^e_{\alpha\beta} e_{\alpha\beta} + \bar{\sigma}^\kappa_{\alpha\beta}\kappa_{\alpha\beta} + \bar{\sigma}^\gamma_\alpha \gamma_\alpha + \bar{\sigma}^\eta_A \eta_A + \bar{\sigma}^{\nabla\eta}_{A\alpha}\eta_{A,\alpha} \tag{24}$$

where, the generalized stresses, $\bar{\sigma}^e_{\alpha\beta}$, $\bar{\sigma}^\kappa_{\alpha\beta}$, $\bar{\sigma}^\gamma_\alpha$, $\bar{\sigma}^\eta_A$, and $\bar{\sigma}^{\nabla\eta}_{A\alpha}$ are the energy conjugates of the corresponding generalized strain components, as indicated in Eq. 24. The generalized stress components are defined as:

$$\begin{aligned}
\bar{\sigma}^{e}_{\alpha\beta} &= \bar{L}^{(ee)}_{\alpha\beta\gamma\eta} e_{\gamma\eta} + \bar{L}^{(e\kappa)}_{\alpha\beta\gamma\eta} \kappa_{\gamma\eta} + \bar{L}^{(e\gamma)}_{\alpha\beta\eta} \gamma_{\eta} + \bar{L}^{(e\nabla\eta)}_{\alpha\beta A\gamma} \eta_{A,\gamma} && \text{(25a)}\\
\bar{\sigma}^{\kappa}_{\alpha\beta} &= \bar{L}^{(\kappa e)}_{\alpha\beta\gamma\eta} e_{\gamma\eta} + \bar{L}^{(\kappa\kappa)}_{\alpha\beta\gamma\eta} \kappa_{\gamma\eta} + \bar{L}^{(\kappa\gamma)}_{\alpha\beta\eta} \gamma_{\eta} + \bar{L}^{(\kappa\nabla\eta)}_{\alpha\beta A\gamma} \eta_{A,\gamma} && \text{(25b)}\\
\bar{\sigma}^{\gamma}_{\alpha} &= \bar{L}^{(\gamma e)}_{\alpha\beta\rho} e_{\beta\rho} + \bar{L}^{(\gamma\kappa)}_{\alpha\beta\rho} \kappa_{\beta\rho} + \bar{L}^{(\gamma\gamma)}_{\alpha\beta} \gamma_{\beta} + \bar{L}^{(\gamma\nabla\eta)}_{\alpha A\beta} \eta_{A,\beta} && \text{(25c)}\\
\bar{\sigma}^{\eta}_{A} &= \bar{L}^{(\eta\eta)}_{AB} \eta_{B} + \bar{L}^{(\eta\nabla\eta)}_{AB\beta} \eta_{B,\beta} && \text{(25d)}\\
\bar{\sigma}^{\nabla\eta}_{A\alpha} &= \bar{L}^{(\nabla\eta e)}_{A\alpha\beta\rho} e_{\beta\rho} + \bar{L}^{(\nabla\eta\kappa)}_{A\alpha\beta\rho} \kappa_{\beta\rho} + \bar{L}^{(\nabla\eta\gamma)}_{A\alpha\beta} \gamma_{\beta} + \bar{L}^{(\nabla\eta\eta)}_{A\alpha B} \eta_{B} + \bar{L}^{(\nabla\eta\nabla\eta)}_{A\alpha B\beta} \eta_{B,\beta} && \text{(25e)}
\end{aligned}$$

in which, the generalized elastic moduli are given as:

$$\begin{aligned}
\bar{L}^{(ee)}_{\alpha\beta\gamma\eta} &= \left\langle L_{\alpha\beta kl} : A^{1}_{kl\gamma\eta} \right\rangle; \quad \bar{L}^{(e\kappa)}_{\alpha\beta\gamma\eta} = \left\langle L_{\alpha\beta kl} : A^{2}_{kl\gamma\eta} \right\rangle; \quad \bar{L}^{(e\gamma)}_{\alpha\beta\eta} = \left\langle L_{\alpha\beta kl} : A^{3}_{kl\eta} \right\rangle && \text{(26a)}\\
\bar{L}^{(\kappa\kappa)}_{\alpha\beta\gamma\eta} &= \left\langle -z L_{\gamma\eta kl} : A^{2}_{kl\alpha\beta} \right\rangle; \quad \bar{L}^{(\kappa\gamma)}_{\alpha\beta\eta} = \left\langle -z L_{\alpha\beta kl} : A^{3}_{kl\eta} \right\rangle \quad \bar{L}^{(\gamma\gamma)}_{\alpha\beta} = \left\langle L_{\alpha 3kl} : A^{3}_{kl\beta} \right\rangle && \text{(26b)}\\
\bar{L}^{(e\nabla\eta)}_{\alpha\beta A\gamma} &= \left\langle A^{1}_{kl\alpha\beta} L_{klj\gamma} H_{jA} \right\rangle; \quad \bar{L}^{(\kappa\nabla\eta)}_{\alpha\beta A\gamma} = \left\langle A^{2}_{kl\alpha\beta} L_{klj\gamma} H_{jA} \right\rangle; \quad \bar{L}^{(\gamma\nabla\eta)}_{\alpha A\beta} = \left\langle A^{1}_{kl\alpha} L_{klj\beta} H_{jA} \right\rangle && \text{(26c)}\\
\bar{L}^{(\eta\eta)}_{AB} &= \left\langle G_{ijA} L_{ijkl} G_{klB} \right\rangle; \quad \bar{L}^{(\eta\nabla\eta)}_{AB\beta} = \left\langle G_{ijA} L_{ijk\beta} H_{kB} \right\rangle; \quad \bar{L}^{(\nabla\eta\nabla\eta)}_{A\alpha B\beta} = \left\langle H_{iA} L_{i\alpha k\beta} H_{kB} \right\rangle && \text{(26d)}
\end{aligned}$$

and;

$$\begin{gathered}
\bar{L}^{(\kappa e)}_{\gamma\eta\alpha\beta} = \bar{L}^{(e\kappa)}_{\alpha\beta\gamma\eta}; \quad \bar{L}^{(\gamma e)}_{\eta\alpha\beta} = \bar{L}^{(e\gamma)}_{\alpha\beta\eta}; \quad \bar{L}^{(\gamma\kappa)}_{\eta\alpha\beta} = \bar{L}^{(\kappa\gamma)}_{\alpha\beta\eta}; \quad \bar{L}^{(\nabla\eta e)}_{A\gamma\alpha\beta} = \bar{L}^{(e\nabla\eta)}_{\alpha\beta A\gamma}\\
\bar{L}^{(\nabla\eta\kappa)}_{A\gamma\alpha\beta} = \bar{L}^{(\kappa\nabla\eta)}_{\alpha\beta A\gamma}; \quad \bar{L}^{(\nabla\eta\gamma)}_{A\beta\alpha} = \bar{L}^{(\gamma\nabla\eta)}_{\alpha A\beta}; \quad \bar{L}^{(\nabla\eta\eta)}_{B\beta A} = \bar{L}^{(\eta\nabla\eta)}_{AB\beta}
\end{gathered} \tag{27}$$

The RVE average of the elastic strain energy is expressed in terms of the generalized macroscopic stress and strains in Eq. 24. In the matrix form, the macroscopic constitutive relationship is expressed as:

$$\bar{\boldsymbol{\sigma}} = \bar{\mathbf{L}}\bar{\boldsymbol{\epsilon}} \tag{28}$$

in which, the generalized tensor of elastic moduli is:

$$\bar{\mathbf{L}} = \begin{bmatrix}
\bar{\mathbf{L}}^{(ee)} & \bar{\mathbf{L}}^{(e\kappa)} & \bar{\mathbf{L}}^{(e\gamma)} & \mathbf{0} & \bar{\mathbf{L}}^{(e\nabla\eta)}\\
\bar{\mathbf{L}}^{(\kappa e)} & \bar{\mathbf{L}}^{(\kappa\kappa)} & \bar{\mathbf{L}}^{(\kappa\gamma)} & \mathbf{0} & \bar{\mathbf{L}}^{(\kappa\nabla\eta)}\\
\bar{\mathbf{L}}^{(\gamma e)} & \bar{\mathbf{L}}^{(\gamma\kappa)} & \bar{\mathbf{L}}^{(\gamma\gamma)} & \mathbf{0} & \bar{\mathbf{L}}^{(\gamma\nabla\eta)}\\
\mathbf{0} & \mathbf{0} & \mathbf{0} & \bar{\mathbf{L}}^{(\eta\eta)} & \bar{\mathbf{L}}^{(\eta\nabla\eta)}\\
\bar{\mathbf{L}}^{(\nabla\eta e)} & \bar{\mathbf{L}}^{(\nabla\eta\kappa)} & \bar{\mathbf{L}}^{(\nabla\eta\gamma)} & \bar{\mathbf{L}}^{(\nabla\eta\eta)} & \bar{\mathbf{L}}^{(\nabla\eta\nabla\eta)}
\end{bmatrix} \tag{29}$$

The components of the generalized macroscopic tensor of elastic moduli are the matrix form of the elastic moduli tensors provided in Eq. 26. By this approach, the strain field is related to the unknown displacement coordinate vector with a macroscopic relationship, $\bar{\boldsymbol{\mathcal{B}}} = \left\{\bar{\boldsymbol{\mathcal{B}}}_1, \bar{\boldsymbol{\mathcal{B}}}_2, \ldots, \bar{\boldsymbol{\mathcal{B}}}_{n_{en}}\right\}$ such that:

$$\bar{\boldsymbol{\mathcal{B}}}_a = \begin{bmatrix}
\boldsymbol{\mathcal{B}}^{e}_{a} & \mathbf{0}\\
\boldsymbol{\mathcal{B}}^{\kappa}_{a} & \mathbf{0}\\
\boldsymbol{\mathcal{B}}^{\gamma}_{a} & \mathbf{0}\\
\mathbf{0} & \boldsymbol{\mathcal{B}}^{\eta}_{a}\\
\mathbf{0} & \boldsymbol{\mathcal{B}}^{\eta,1}_{a}\\
\mathbf{0} & \boldsymbol{\mathcal{B}}^{\eta,2}_{a}
\end{bmatrix} \tag{30}$$

with, $\boldsymbol{\mathcal{B}}^{\eta}_{a} = \mathbf{I}N_a$; $\boldsymbol{\mathcal{B}}^{\eta,\alpha}_{a} = \mathbf{I}N_{a,\alpha}$, and; $\mathbf{I}$ is the identity matrix. By this approach, the element stiffness matrix can be expressed as:

$$\mathbf{K}^e = \sum_{I=1}^{n_{int}} W_I J_I \bar{\boldsymbol{\mathcal{B}}}^T \bar{\mathbf{L}} \bar{\boldsymbol{\mathcal{B}}} \tag{31}$$

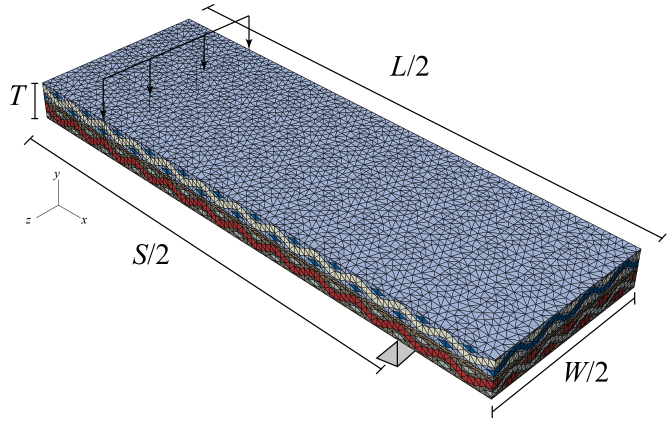

Figure 3: The geometry of the four-point bending plate problem.

The proposed homogenization operation and the HLI integration scheme leads to identical stiffness matrices. The proposed scheme is computationally advantageous since no RVE level integration is required as $\bar{\boldsymbol{\mathcal{B}}}$ and $\bar{\mathbf{L}}$ are functions of macroscopic coordinates only.

3.4 Numerical Verification

The proposed multiscale model is verified using a four-point plate bending problem. A quarter of the plate geometry is illustrated in Fig. 3. The dimensions of the plate are $L = 28.23$mm, $W = 9.41$mm, and $T = 1$mm where, L, W, and T denote the length, width, and the thickness of the plate, respectively. The microstructure consists of two woven composite layers separated by a thin interphase. The laminate and interphase thicknesses are 0.47 and 0.06mm, respectively. The interphase has identical properties with the composite matrix material. The elastic moduli of the reinforcement and matrix materials are 60 GPa and 3 GPa, respectively. The Poisson's ratio for both of the materials is 0.35. Numerical simulations with span-to-thickness ratios, $S/T = 23.52$ and $S/T = 18.82$ are conducted to verify the proposed multiscale model. Along the transverse direction, forces with the amplitude 9.62 N/mm and 19.24 N/mm are applied in $S/T = 23.52$ and $S/T = 18.82$ simulations, respectively. The vertical deflection profile predicted by the proposed multiscale model for $S/T = 23.52$ is compared with the predictions of a full 3-D finite element analysis (mesh shown in Fig. 3), and two Abaqus shell models in Fig. 4. Abaqus S8R model employs the standard 8-noded quadrilateral shell elements with the homogenized material properties of the RVE, which consists of the two-woven layers and the interphase. The homogenized properties are obtained by evaluating the IFP1 problem using periodic boundary conditions at all directions:

$$L_{ijkl}^{\mathrm{hom}} = \frac{1}{|\mathcal{Y}_x|} \int_{\mathcal{Y}_x} L_{ijmn} A_{mnkl}^{1} d\mathcal{Y} \tag{32}$$

The non-zero values of the homogenized stiffness tensor, L_{ijkl}^{hom}, are provided in Table 1. In S8R-Composite model, numerical integration is employed in the thickness direction. Each woven-composite layer and the interphase are treated as separate layers in the through-thickness integration. The homogenized properties of the woven composite layer are computed by evaluating the IFP1 problem a periodic woven composite unit cell. The homogenized properties of the composite laminate are summarized in Table 1. Figure 4 shows that the displacement is predicted using the proposed multiscale model with excellent accuracy (within 1.6%).

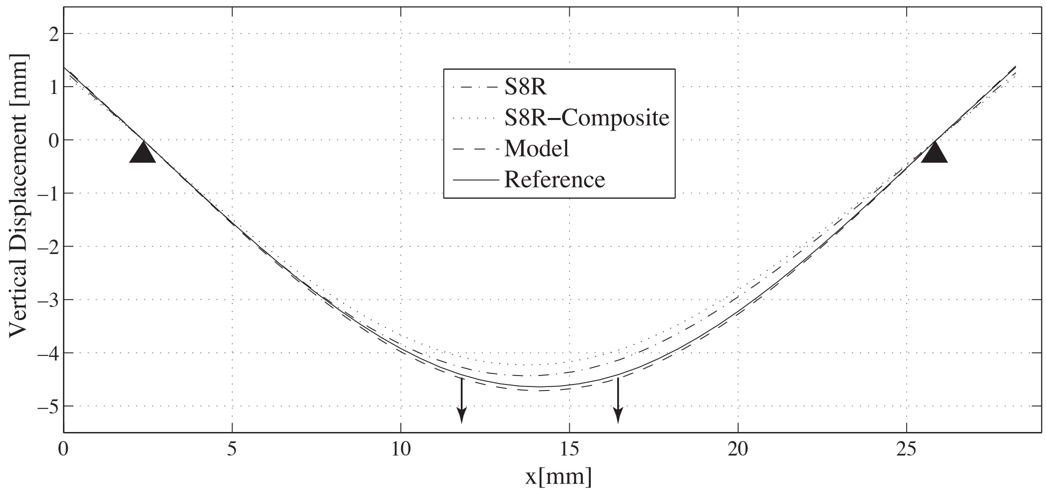

Figure 4: The displacement profiles of the 4-point bending of the plate as computed by Abaqus models, the proposed model and the reference three dimensional model.

Table 1: Homogenized material properties employed in Abaqus model analyses

	L^{hom}_{1111}	L^{hom}_{1122}	L^{hom}_{2222}	L^{hom}_{1212}	L^{hom}_{1313}	L^{hom}_{2323}
RVE	1.5123e4	2.7245e3	1.1185e4	3.7190e3	2.2074e3	2.2100e3
Laminate	1.5795e4	2.7732e3	1.1566e4	3.8803e3	2.3590e3	2.3669e3

The relative maximum error of the proposed model and the Abaqus models compared to the reference model are summarized in Table 2. The proposed model predicts the bending response with excellent accuracy.

4 Multiscale Enrichment of the Nonlinear Heterogeneous Plates

In this section, the two-level enrichment methodology is extended to the problems with material nonlinearity. The formulation of the enrichment methodology is presented in the context of failure modeling. Implementation details and numerical verifications are provided.

Table 2: Performance of the proposed multiscale model in the 4-point bending of elastic unidirectionally reinforced plate

	$S/T = 23.52$		$S/T = 18.82$	
Source	u_3	error %	u_3	error %
Reference	4.64005	-	4.6708	-
Model	4.7121	1.55	4.7430	1.55
S8R	4.4051	5.06	4.4560	3.96
S8R-Composite	4.2137	9.19	4.2634	8.72

4.1 Formulation

The constitutive equation of the 3-D nonlinear boundary value problem is expressed as follows:

$$\sigma_{ij}(\mathbf{x}) = L_{ijkl}(\mathbf{x})\left[\epsilon_{kl}(\mathbf{x}) - \mu_{kl}(\mathbf{x})\right] \tag{33}$$

where, μ_{ij} denotes the inelastic strain field. The inelastic strain field reflects the effects of plastic, thermal, damage or other processes. In this manuscript, we restrict our attention to the failure response of brittle heterogeneous materials. The failure response is modeled using continuum damage mechanics. The inelastic strain component then takes the form:

$$\mu_{ij}(\mathbf{x}) = \omega(\mathbf{x})\,\epsilon_{ij}(\mathbf{x}) \tag{34}$$

where, $\omega \in [0,1]$ is a nonlinear history dependent damage variable with $\omega = 0$ corresponding to the state of no damage, and $\omega = 1$ representing a complete loss of load carrying capacity. The enriched displacement field decomposition is identical to the linear case and provided by Eq. 6. The strain tensor is expressed as:

$$\epsilon_{ij}(\mathbf{x}) = \mathcal{A}^1_{ij\alpha\beta}(\mathbf{x})\,e_{\alpha\beta}(x) + \mathcal{A}^2_{ij\alpha\beta}(\mathbf{x})\,\kappa_{\alpha\beta}(x) + \mathcal{A}^3_{ij\alpha}(\mathbf{x})\,\gamma_\alpha(x) + \hat{\epsilon}_{ij}(\mathbf{x}) \tag{35}$$

with the secant concentration tensors:

$$\mathcal{A}^1_{ij\alpha\beta} = I_{ij\alpha\beta} + \mathcal{G}^1_{ij\alpha\beta}; \quad \mathcal{A}^2_{ij\alpha\beta} = -zI_{ij\alpha\beta} + \mathcal{G}^2_{ij\alpha\beta}; \quad \mathcal{A}^3_{ij\alpha} = I_{ij\alpha 3} + \mathcal{G}^1_{ij\alpha 3}; \tag{36}$$

where, $\mathcal{G}^p_{ijkl} = \mathcal{H}^p_{(i,j)kl}$, $p = 1,2$ are the secant polarization tensors.

The enrichment functions $\mathcal{H}^p_{ikl}$ vary with the evolution of the inelastic strains. The boundary value problem of the classical mathematical homogenization theory yields the nonlinear enrichment functions, $\mathcal{H}^p_{ikl}$.

NIFP: Nonlinear Influence Function Problem:

$$\left[L_{ijmn}\left(\mathcal{H}^1_{(m,n)\alpha\beta}e_{\alpha\beta} + I_{mn\alpha\beta}e_{\alpha\beta} - \mu^e_{mn}\right)\right]_{,j} = 0 \quad \text{on } \mathcal{Y}_x \tag{37a}$$

$$\left[L_{ijmn}\left(\mathcal{H}^2_{(m,n)\alpha\beta}\kappa_{\alpha\beta} - zI_{mn\alpha\beta}\kappa_{\alpha\beta} - \mu^\kappa_{mn}\right)\right]_{,j} = 0 \quad \text{on } \mathcal{Y}_x \tag{37b}$$

$$\left[L_{ijmn}\left(\mathcal{H}^1_{(m,n)\alpha 3}\gamma_\alpha + I_{mn\alpha 3}\gamma_\alpha - \mu^\gamma_{mn}\right)\right]_{,j} = 0 \quad \text{on } \mathcal{Y}_x \tag{37c}$$

$$\mu^e_{ij} = \omega\mathcal{A}^1_{ij\alpha\beta}e_{\alpha\beta}; \quad \mu^\kappa_{ij} = \omega\mathcal{A}^2_{ij\alpha\beta}\kappa_{\alpha\beta}; \quad \mu^\gamma_{ij} = \omega\mathcal{A}^3_{ij\alpha}\gamma_\alpha \tag{37d}$$

$$\mathcal{H}^p_{ikl}\ \mathbf{x}\text{-periodic on } \partial\mathcal{Y}^{\text{per}}_x; \quad \mathcal{H}^p_{ikl}\ x\text{-periodic on } \partial\mathcal{Y}^{\text{z}}_x \tag{37e}$$

$$e^z_i L_{ijmn}\left(\mathcal{H}^p_{(m,n)kl} + (-z)^{p-1}I_{mnkl}\right)n_j = 0 \text{ on } \partial\mathcal{Y}^{\text{z}}_x \tag{37f}$$

where, $\mu_{ij} = \mu^e_{ij} + \mu^\kappa_{ij} + \mu^\gamma_{ij}$.

Evaluation of the macroscale plate problem by using the enrichment functions defined above poses a significant computational challenge. For instance, when the HLI integration scheme is utilized, the NIFP problem must be evaluated at each integration point of the macroscale finite element mesh during each iteration and increment of the macroscale problem. In case of a full integration scheme, the computational complexity increases as the number of RVEs describing the macroscopic domain increases. An efficient way to circumvent this problem is to use the eigendeformation-based model reduction methodology. The eigendeformation based model reduction methodology hinges on expressing the solution field as a superposition of linear influence functions and representing the inelastic fields in terms of these linear functions.

Ref. [23] provides a detailed account of the eigendeformation based model reduction methodology. In this work, this methodology is applied in the context of heterogeneous plates. By this approach, the strain field is expressed using only the elastic strain concentration tensors:

$$\epsilon_{ij}(\mathbf{x}) = A^1_{ij\alpha\beta}(\mathbf{x})\, e_{\alpha\beta}(x) + A^2_{ij\alpha\beta}(\mathbf{x})\, \kappa_{\alpha\beta}(x) + A^3_{ij\alpha}(\mathbf{x})\, \gamma_\alpha(x) + \tilde{\epsilon}_{ij}(\mathbf{x}) + \hat{\epsilon}_{ij}(\mathbf{x}) \tag{38}$$

where,

$$\tilde{\epsilon}_{ij}(\mathbf{x}) = \int_{\mathcal{Y}_x} g_{ijkl}(\hat{\mathbf{x}}, \mathbf{x})\, \mu_{kl}(\hat{\mathbf{x}})\, d\hat{\mathbf{x}} \tag{39}$$

$g_{ijkl} = h_{(i,j)kl}$, and; h_{ikl} are the influence functions induced by the inelastic deformations. The inelastic strain induced influence functions are obtained by evaluating the following linear-elastic RVE problem for every point $\hat{\mathbf{x}}$ within the RVE.

ISIF: Inelastic Strain Induced Influence Function Problem:

$$\left[L_{ijmn}\left(h_{(m,n)kl}(\mathbf{x}, \hat{\mathbf{x}}) - d(\mathbf{x} - \hat{\mathbf{x}})\, I_{mnkl}\right)\right]_{,j} = 0 \quad \mathbf{x}, \hat{\mathbf{x}} \text{ on } \mathcal{Y}_x \tag{40a}$$

$$h_{ikl}\ \mathbf{x}\text{-periodic on } \partial\mathcal{Y}_x^{\mathrm{per}}; \quad h_{ikl}\ x\text{-periodic on } \partial\mathcal{Y}_x^{\mathrm{z}} \tag{40b}$$

$$e_i^z L_{ijmn}\left(h_{(m,n)kl}(\mathbf{x}, \hat{\mathbf{x}}) - d(\mathbf{x} - \hat{\mathbf{x}})\, I_{mnkl}\right) n_j = 0 \text{ on } \partial\mathcal{Y}_x^{\mathrm{z}} \tag{40c}$$

in which, d is the Dirac delta distribution. The influence function problem, ISIF, is evaluated numerically by replacing the Dirac distribution with a function approximation [23].

It is also possible to use a *dynamic* enrichment strategy to describe the displacement field by replacing the linear enrichment functions H_{iA} with $\mathcal{H}_{iA}$ in Eq. 6. This approach leads to a non-standard non-local formulation. In this approach the enrichment functions computed at the integration points (using the HLI scheme) neighboring an enriched nodes must be interpolated to compute the enrichment function at the enriched node. Since, the inelastic fields associated with all elements neighboring the node contribute to the form of the enrichment function, the constitutive response and the resulting formulation is non-local. In contrast, the displacement field introduced in Eq. 6 leads to a numerical formulation that lies within the standard finite element framework.

4.2 Computational Aspects

The discretization of the macroscopic displacement components for the nonlinear problem is identical to the linear problem, and described in Eq. 11. We proceed by the discretization of the inelastic strain field, μ_{ij}, and the damage variable, ω:

$$\{\omega, \mu_{ij}\}(\mathbf{x}) = \sum_I N_{\mathrm{ph}}^{(I)}(\mathbf{x}) \left\{\omega^{(I)}, \mu_{ij}^{(I)}\right\}(x); \quad I = 1, 2, \ldots \tag{41}$$

where, $N_{\mathrm{ph}}^{(I)}$ are shape functions and, $\mu_{ij}^{(I)}$ and $\omega^{(I)}$ are interpreted as weighted phase average of the respective fields over the RVE at position $\mathbf{x}$.

$$\left\{\omega^{(I)}, \mu_{ij}^{(I)}\right\}(x) = \int_{\mathcal{Y}_x} \psi^{(I)}(\mathbf{x})\, \{\omega, \mu_{ij}\}(\mathbf{x}) d\mathcal{Y} \tag{42}$$

$\mu_{ij}^{(I)}$ and $\omega^{(I)}$ are constant within the RVE but vary from one RVE to the next. The shape and weight functions $N_{\mathrm{ph}}^{(I)}$ and $\psi^{(I)}$, respectively are taken to be piecewise constant within the

RVE:

$$N_{\mathrm{ph}}^{(I)}(\mathbf{x}) = \begin{cases} 1 & \text{if } \mathbf{x} \in \mathcal{Y}_x^{(I)} \\ 0 & \text{elsewhere} \end{cases} \tag{43}$$

$$\psi^{(I)}(\mathbf{x}) = \frac{1}{|\mathcal{Y}_x^{(I)}|} N_{\mathrm{ph}}^{(I)}(\mathbf{x}) \tag{44}$$

where, $\mathcal{Y}_x^{(I)}$ denotes non-overlapping subdomains of the RVE at position $\mathbf{x}$. Therefore, if the RVE at position $\mathbf{x}$ is decomposed into n non-overlapping partitions ($I = 1, 2, \ldots, n$), it is sufficient to evaluate n weighted phase average inelastic strains to define the deformation of the structure. The resulting model is called an n-partition model.

The weighted phase average inelastic strain field is related to the weighted phase average damage and strain by substituting Eq. 41 into Eq. 34 and using Eq. 42:

$$\mu_{ij}^{(I)}(x) = \omega^{(I)}(x)\, \epsilon_{ij}^{(I)}(x) \tag{45}$$

Combining Eqs. 38, 39 and 45 yields:

$$\begin{aligned} &\sum_{J=1}^{n} \left[I_{ijkl}\delta_{IJ} - \omega^{(I)}(x)\, P_{ijkl}^{(IJ)} \right] \mu_{kl}^{(J)}(x) = \omega^{(I)}(x) \times \\ &\quad \times \left(A_{ij\alpha\beta}^{1(I)} e_{\alpha\beta}(x) + A_{ij\alpha\beta}^{2(I)} \kappa_{\alpha\beta}(x) + A_{ij\alpha}^{3(I)} \gamma_\alpha(x) + \hat{\epsilon}_{ij}^{(I)} \right); \quad I = 1, 2, \ldots, n \end{aligned} \tag{46}$$

where, δ_{IJ} is the Kronecker delta, and;

$$P_{ijkl}^{(IJ)}(x) = \int_{\mathcal{Y}_x^{(I)}} \tilde{P}_{ijkl}^{(J)}(\mathbf{x})\, d\mathcal{Y} \tag{47}$$

$$A_{ijkl}^{p(I)}(x) = \frac{1}{|\mathcal{Y}_x^{(I)}|} \int_{\mathcal{Y}_x^{(I)}} A_{ijkl}^{p}(\mathbf{x})\, d\mathcal{Y} \tag{48}$$

$$\hat{\epsilon}_{ij}^{(I)}(x) = \frac{1}{|\mathcal{Y}_x^{(I)}|} \int_{\mathcal{Y}_x^{(I)}} \hat{\epsilon}_{ij}(\mathbf{x})\, d\mathcal{Y} \tag{49}$$

and,

$$\tilde{P}_{ijkl}^{(J)}(\mathbf{x}) = \frac{1}{|\mathcal{Y}_x^{(J)}|} \int_{\mathcal{Y}_x^{(J)}} g_{ijkl}(\mathbf{x}, \hat{\mathbf{x}})\, d\hat{\mathcal{Y}} \tag{50}$$

When put in a matrix form, Eq. 46 results in a nonlinear system of equations, which may be evaluated to compute the constitutive response:

$$\Phi(\mathbf{d}) = \mathbf{K}(\mathbf{d})\, \mathbf{d} - \mathbf{f} = \mathbf{0} \tag{51}$$

in which,

$$\mathbf{d} = \left\{ \boldsymbol{\mu}^{(1)}, \boldsymbol{\mu}^{(2)}, \ldots, \boldsymbol{\mu}^{(n)} \right\}^{\mathrm{T}} \tag{52}$$

$$\mathbf{K} = \begin{bmatrix} \mathbf{I} - \mathbf{P}^{(11)}\omega^{(1)} & -\mathbf{P}^{(12)}\omega^{(1)} & \cdots & -\mathbf{P}^{(1n)}\omega^{(1)} \\ -\mathbf{P}^{(21)}\omega^{(2)} & \mathbf{I} - \mathbf{P}^{(22)}\omega^{(2)} & \cdots & -\mathbf{P}^{(2n)}\omega^{(2)} \\ \vdots & \vdots & \ddots & \vdots \\ -\mathbf{P}^{(n1)}\omega^{(n)} & -\mathbf{P}^{(n2)}\omega^{(n)} & \cdots & \mathbf{I} - \mathbf{P}^{(nn)}\omega^{(n)} \end{bmatrix} \tag{53}$$

$$\mathbf{f}\left(\mathbf{d}\right)=\left\{\omega^{(1)}\boldsymbol{\mathcal{B}}^{(1)};\omega^{(2)}\boldsymbol{\mathcal{B}}^{(2)};\ldots\omega^{(n)}\boldsymbol{\mathcal{B}}^{(n)}\right\}\mathbf{c}=\mathbf{Qc} \tag{54}$$

The components of the $\boldsymbol{\mathcal{B}}^{(I)}=\left\{\boldsymbol{\mathcal{B}}_1^{(I)},\boldsymbol{\mathcal{B}}_2^{(I)},\ldots,\boldsymbol{\mathcal{B}}_{n_{en}}^{(I)}\right\}$ are expressed as:

$$\boldsymbol{\mathcal{B}}_a^{(I)}\left(x\right)=\left[\begin{array}{c|c}\mathbf{A}^{1(I)}\mathbf{B}_a^e+\mathbf{A}^{2(I)}\mathbf{B}_a^\kappa+\mathbf{A}^{3(I)}\mathbf{B}_a^\gamma & \hat{\mathbf{G}}_a^{(I)}\left(x\right)\end{array}\right] \tag{55}$$

The components of the $\hat{\mathbf{G}}_a^{(I)}$ are obtained by weighted averaging of the corresponding components of $\hat{\mathbf{G}}_a$ over the RVE partition, I. Finally, the strains can be expressed in terms of the unknown vector $\mathbf{c}$ by substituting the inelastic strain field discretization provided in Eq. 41 and solution of Eq. 51 into Eq. 38:

$$\boldsymbol{\epsilon}=\mathbf{Bc}=\left(\boldsymbol{\mathcal{B}}+\mathbf{MK}^{-1}\mathbf{Q}\right)\mathbf{c} \tag{56}$$

where,

$$\mathbf{M}_I\left(\mathbf{x}\right)=\left\{\tilde{\mathbf{P}}^{(1)},\tilde{\mathbf{P}}^{(2)},\ldots,\tilde{\mathbf{P}}^{(n)}\right\} \tag{57}$$

4.2.1 Integration Algorithm

The general structure of the multiscale enrichment methodology implementation is illustrated in Fig. 5. The proposed methodology is incorporated into the commercial finite element program Abaqus using the user element subroutine utility (UEL). The implementation of the methodology consists of the preprocessing stage, and computation of the element matrices in UEL. In the preprocessing stage, the elastic and damage influence functions are computed by solving the IFP1, IFP2, and ISIF problems presented above. The linearity of the influence function problems permits their computation prior to macroscopic analysis. The coefficient tensors used in the stress integration and evaluation of the enrichment functions are computed at the preprocessing stage as well. The computation of the coefficient tensors consists of three steps: (1) selection of the model order, n; (2) partitioning of the RVE based on the model order, and; (3) evaluation of the integral forms to obtain the coefficient tensors. Various partitioning strategies including the dynamic partitioning strategy, in which the number of partitions are taken as a function of the damage state, and the static partitioning strategy, in which number of partitions are taken to be constant at an RVE throughout the macroscopic analysis are presented in Ref. [23]. In this section, we focus on the computation of the macroscopic response given the coefficient tensors.

The microscopic response within a macroscopic finite element is evaluated by a simple update algorithm. We present the computation of the element level stiffness matrix and force vectors only. The global matrices can be evaluated using standard finite element assembly procedures. The steps of the proposed algorithm are described below:
Given: the displacement coefficients ${}_n\mathbf{c}$, damage and inelastic strain states, ${}_n\omega^{(I)}$ and ${}_n\boldsymbol{\mu}^{(I)}$, respectively, at the equilibrium state at time t_n, and; the displacement coefficient increments, $\Delta\mathbf{c}$.
Calculate: the updated damage and inelastic state variables ${}_{n+1}\omega^{(I)}$ and ${}_{n+1}\boldsymbol{\mu}^{(I)}$, respectively; internal force and tangent stiffness matrix at the current equilibrium state at time t_{n+1}.

In what follows, a left subscript n denotes the value at time t_n. The variables without a left subscript are the current values at time t_{n+1}.
At each macroscopic integration point within the macroscopic finite element:

1. Evaluate $\Phi\left(\mathbf{d}\right)=\mathbf{0}$ using a Newton iteration scheme. by setting the initial guess to ${}_n\mathbf{d}$.

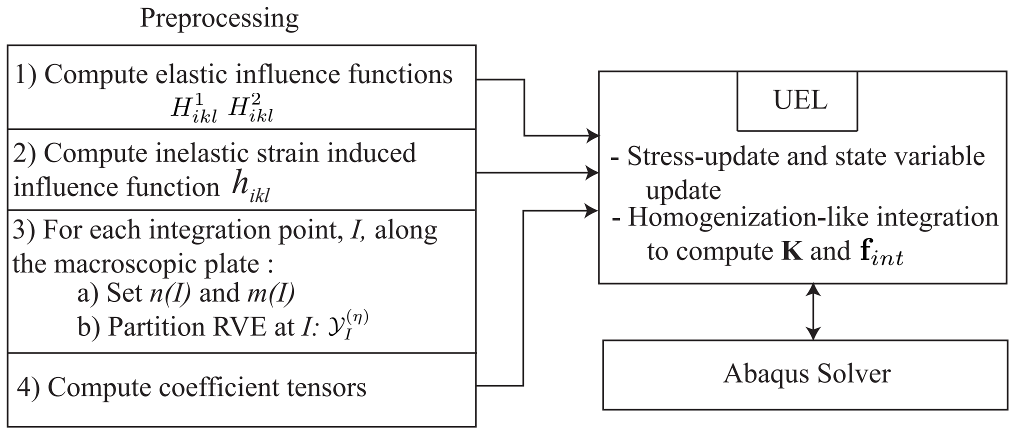

Figure 5: Program Architecture: Preprocessing and element level computations.

2. At each microscopic integration point, compute:
   (a) Strain using Eq. 56.
   (b) Stress using Eq. 33.
   (c) Consistent tangent moduli $\mathbf{L}^t$ such that $\boldsymbol{\sigma} - {}_n\boldsymbol{\sigma} = \mathbf{L}^t \Delta\boldsymbol{\epsilon}$. The strain increment can be computed as $\Delta\boldsymbol{\epsilon} = \mathbf{B}\Delta\mathbf{c}$
3. Integrate over the RVE at the macroscopic integration point to compute the internal force and tangent stiffness matrix based on the homogenization-like integration scheme.

$$\mathbf{f}_{int} = \sum_{I=1}^{n_{int}} W_I J_I \frac{1}{|\mathcal{Y}_I|} \int_{\mathcal{Y}_I} \mathbf{B}^T \boldsymbol{\sigma} d\mathbf{x} \tag{58}$$

$$\mathbf{K} = \sum_{I=1}^{n_{int}} W_I J_I \frac{1}{|\mathcal{Y}_I|} \int_{\mathcal{Y}_I} \mathbf{B}^T \boldsymbol{\mathcal{L}} \mathbf{B} d\mathbf{x} \tag{59}$$

where, W_I is the weighting factors; J_I the jacobian, and $\mathcal{Y}_I$ is the RVE positioned at the integration point, I.

4.3 HLI-Free Homogenization Operator for Nonlinear Multiscale Enrichment

In this section, the homogenization operator proposed for the linear problems in Section 3.3 is extended to nonlinear problems. The generalized stress components is related to the stress tensor by the following relationships:

$$\bar{\sigma}^e_{\alpha\beta} = \left\langle A^1_{kl\alpha\beta}\sigma_{kl}\right\rangle; \quad \bar{\sigma}^\kappa_{\alpha\beta} = \left\langle A^2_{kl\alpha\beta}\sigma_{kl}\right\rangle; \quad \bar{\sigma}^\gamma_{\alpha} = \left\langle A^3_{kl\alpha}\sigma_{kl}\right\rangle \tag{60a}$$

$$\bar{\sigma}^\eta_A = \left\langle G_{klA}\sigma_{kl}\right\rangle; \quad \bar{\sigma}^{\nabla\eta}_{A\alpha} = \left\langle H_{kA}\sigma_{k\alpha}\right\rangle \tag{60b}$$

First consider the macroscopic in-plane stresses $\bar{\sigma}^e_{\alpha\beta}$. In the presence of nonlinearities, the macroscopic in-plane stresses is expressed in terms of the generalized macroscopic strains and the eigenstrains by substituting Eqs. 9, 33, 39, 41 and 50 into the above equation:

$$\bar{\sigma}^e_{\alpha\beta} = \bar{L}^{(ee)}_{\alpha\beta\gamma\eta} e_{\gamma\eta} + \bar{L}^{(e\kappa)}_{\alpha\beta\gamma\eta}\kappa_{\gamma\eta} + \bar{L}^{(e\gamma)}_{\alpha\beta\eta}\gamma_\eta + \bar{L}^{(e\nabla\eta)}_{\alpha\beta A\gamma}\eta_{A,\gamma} + \sum_{I=1}^{n} M^{e(I)}_{ijkl}\mu^{(I)}_{kl} \tag{61}$$

in which,

$$M_{ijkl}^{e(I)} = \left\langle A_{mnij}^{1} L_{mnpq} \left(\tilde{P}_{pqkl}^{(I)} - I_{pqkl} N_{\mathrm{ph}} \right) \right\rangle \tag{62}$$

Using the same procedure for the remainder of the generalized stress components leads to the constitutive relationship between the generalized stress, strain and eigenstrain. In the matrix form, the macroscopic constitutive relationship is expressed as:

$$\bar{\boldsymbol{\sigma}} = \bar{\mathbf{L}} \bar{\boldsymbol{\epsilon}} + \sum_{I=1}^{n} \mathbf{M}^{(I)} \boldsymbol{\mu}^{(I)} \tag{63}$$

where,

$$\mathbf{M}^{(I)} = \left[\mathbf{M}^{e(I)}, \, \mathbf{M}^{\kappa(I)}, \, \mathbf{M}^{\gamma(I)}, \, \mathbf{M}^{\eta(I)}, \, \mathbf{M}^{\nabla\eta(I)} \right]^{T} \tag{64}$$

and,

$$M_{ijkl}^{\kappa(I)} = \left\langle A_{mnij}^{2} L_{mnpq} \left(\tilde{P}_{pqkl}^{(I)} - I_{pqkl} N_{\mathrm{ph}}^{(I)} \right) \right\rangle; \; M_{\alpha kl}^{\gamma(I)} = \left\langle A_{mn\alpha}^{3} L_{mnpq} \left(\tilde{P}_{pqkl}^{(I)} - I_{pqkl} N_{\mathrm{ph}}^{(I)} \right) \right\rangle \tag{65a}$$

$$M_{Akl}^{\eta(I)} = \left\langle G_{mnA} L_{mnpq} \left(\tilde{P}_{pqkl}^{(I)} - I_{pqkl} N_{\mathrm{ph}}^{(I)} \right) \right\rangle; \; M_{A\alpha kl}^{\nabla\eta(I)} = \left\langle H_{mA} L_{m\alpha pq} \left(\tilde{P}_{pqkl}^{(I)} - I_{pqkl} N_{\mathrm{ph}}^{(I)} \right) \right\rangle \tag{65b}$$

By this formulation, the computation of the tangent stiffness and force vectors are simplified. The steps of the proposed algorithm are described below:
Given: the displacement coefficients ${}_{n}\mathbf{c}$, damage and inelastic strain states, ${}_{n}\omega^{(I)}$ and ${}_{n}\boldsymbol{\mu}^{(I)}$, respectively, at the equilibrium state at time t_n, and; the displacement coefficient increments, $\Delta\mathbf{c}$.
Calculate: the updated damage and inelastic state variables ${}_{n+1}\omega^{(I)}$ and ${}_{n+1}\boldsymbol{\mu}^{(I)}$, respectively; internal force and tangent stiffness matrix at the current equilibrium state at time t_{n+1}.

At each macroscopic integration point within the macroscopic finite element:

1. Evaluate $\Phi(\mathbf{d}) = \mathbf{0}$ using a Newton iteration scheme. by setting the initial guess to ${}_{n}\mathbf{d}$.
2. Compute stress using Eq. 63
3. Compute Consistent tangent moduli $\bar{\mathbf{L}}^{t}$ such that $\bar{\boldsymbol{\sigma}} - {}_{n}\bar{\boldsymbol{\sigma}} = \bar{\mathbf{L}}^{t} \Delta\bar{\boldsymbol{\epsilon}}$.
4. Compute the force and tangent stiffness matrix:

$$\mathbf{f}^{e} = \sum_{I=1}^{n_{int}} W_I J_I \bar{\boldsymbol{\mathcal{B}}}^{T} \bar{\boldsymbol{\sigma}}; \quad \mathbf{K}^{e} = \sum_{I=1}^{n_{int}} W_I J_I \bar{\boldsymbol{\mathcal{B}}}^{T} \bar{\mathbf{L}}^{t} \bar{\boldsymbol{\mathcal{B}}} \tag{66}$$

4.4 Damage Evolution Model

The evolution of damage within the microconstituents and along the interfaces is modeled using a rate-dependent continuous damage mechanics model. Consider a damage potential function such that

$$f\left(\upsilon^{(I)}, r^{(I)}\right) = \phi\left(\upsilon^{(I)}\right) - \phi\left(r^{(I)}\right) \leqslant 0 \tag{67}$$

where, ϕ is a monotonically increasing damage evolution function. The evolution of the history parameter, $r^{(I)}$ and damage is then expressed in terms of the consistency parameter, λ:

$$\dot{r}^{(I)} = \dot{\lambda} \tag{68}$$

$$\dot{\omega}^{(I)} = \dot{\lambda} \frac{\partial \phi}{\partial \upsilon^{(I)}} \tag{69}$$

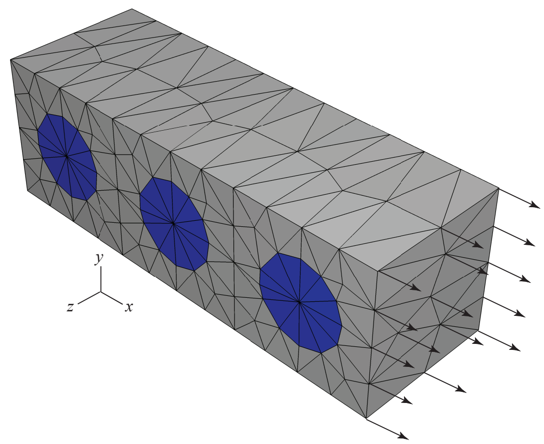

Figure 6: The geometry, loading and discretization of the three-dimensional structure.

The damage accumulation is governed by the Kuhn-Tucker conditions ($\dot{\lambda} \geq 0$; $f \leq 0$; $\dot{\lambda} f = 0$). $\upsilon^{(I)}$ is given in terms of the principal strains as:

$$\upsilon^{(I)} = \sqrt{\frac{1}{2} \left(\mathbf{F} \hat{\boldsymbol{\epsilon}}^{(I)} \right)^{\mathrm{T}} \hat{\mathbf{L}} \left(\mathbf{F} \hat{\boldsymbol{\epsilon}}^{(I)} \right)} \tag{70}$$

in which, $\hat{\boldsymbol{\epsilon}}^{(I)}$ is the principal strain tensor in $\mathcal{Y}_x^{(I)}$; $\hat{\mathbf{L}}$ is the tensor of elastic moduli rotated onto the principal strain directions, and; $\mathbf{F}$ is the weighting matrix that accounts for the anisotropic damage accumulation in tensile and compressive directions:

$$\mathbf{F}^{(\eta)} = \begin{bmatrix} h_1 & 0 & 0 \\ 0 & h_2 & 0 \\ 0 & 0 & h_3 \end{bmatrix} \tag{71}$$

$$h_\xi = \frac{1}{2} + \frac{1}{\pi} \mathrm{atan} \left[c_1 \left(\hat{\epsilon}_\xi^{(I)} - c_2 \right) \right]; \quad \xi = 1, 2, 3 \tag{72}$$

Material parameters, c_1 and c_2 control damage accumulation in the tensile and compressive loading.

4.5 Numerical Verification

4.5.1 Failure due to Uniaxial Loading

The planar deformation performance of the proposed multiscale approach is verified by analyzing the three-dimensional structure illustrated in Fig. 6. The structure is comprised of three unidirectionally reinforced unit cells with a fiber volume fraction of 26.7%. The reinforcements are placed perpendicular to the loading direction. The structure is subjected to uniaxial tension along the x-direction until failure. Perfect adhesion is assumed along the boundaries of the microconstituents. The fibers remain elastic throughout the duration of the loading, with the Young's modulus and Poisson's ratio of 60 MPa and 0.3, respectively. The matrix is taken to accumulate damage during loading. The material parameters describing the damage accumulation along with the elastic parameters are summarized in Table 3.

Table 3: Material property values for the matrix material

E	ν	a_1^{ph}	a_2^{ph}	c_1	c_2	υ_{ini}
60 GPa	0.3	0.3	1.0	1e5	0.0	0.0

The reference solution is provided by three-dimensional finite element analysis with full resolution of the microstructure throughout the structure. The discretization of the three-dimensional reference model is illustrated in Fig. 6. Two separate multiscale (4-partition and 10-partition) models are considered for verification. The macroscopic scale of the multiscale models are discretized using three 4-node quadrilateral shell elements enhanced by multiscale shape functions. The discretization of the microscopic scale is identical to a third of the three-dimensional finite element mesh shown in Fig. 6.

The overall stress-strain response of the multiscale models in addition to the reference simulation is presented in Fig. 7. The stress-strain curves of the multiscale models follow the reference curve closely, indicating that the multiscale models correctly predict the damage evolution within the microstructure as evidenced further in Fig. 8. The stress-to-failure values provided by the multiscale models match reasonably well with the reference model (with an error of 8.39% for 4-partition model, and 6.85% for 10-partition model). While, a 10-partition model predicts the reference state closer than the 4-partition model, it has been previously observed that the model error reduction is not monotonic with the increasing model order [30]. Specifically, a significant increase in model order (i.e., value of n) is typically necessary for further increase in model accuracy. Figure 7 also illustrates the effect of displacement level enrichment on the failure response of the structure. While the predictions of pre-peak strength damage evolution match closely with the proposed multiscale models, the strain-only enrichment overpredicts the post-peak strength. This is in line with the previous investigations that the response of displacement-strain enriched multiscale models reduce to the strain-only enriched models in the presence of smooth fields [12]. Figure 8 illustrates the damage evolution profiles of the 4-partition, 10-partition and reference models. The reported damage values are average over the three unit cells shown in Fig. 6. In all three elements, both of the proposed multiscale models predicts the overall damage evolution within the microstructure with reasonable accuracy.

4.5.2 Failure due to Bending

The bending performance of the proposed multiscale approach is verified against direct finite element simulations using a 4-point plate bending problem. The geometry of the problem is identical to that described in Section 3.4 ($S/W = 16$ case) and shown in Fig 3. The plate is subjected to vertical displacement until failure under bending. The failure of the microstructure is through matrix microcracking only, and the reinforcements are assumed to be elastic. The material parameters describing the failure of the matrix are shown in Table 3.

The predictions of a 4-partition multiscale model are compared to the three-dimensional finite element simulations. The macroscopic mesh of the multiscale model consists of 192 quadrilateral enriched elements while the direct finite element model consists of 67392 tetrahedra. Figure 9 illustrates the reaction force-applied displacement diagrams for the reference and multiscale models. The proposed multiscale model predicted the failure force within 2.1% accuracy. The damage profile for each partition of the multiscale model as well as the reference simulation is provided in Fig. 10. Damage accumulation characteristics predicted using

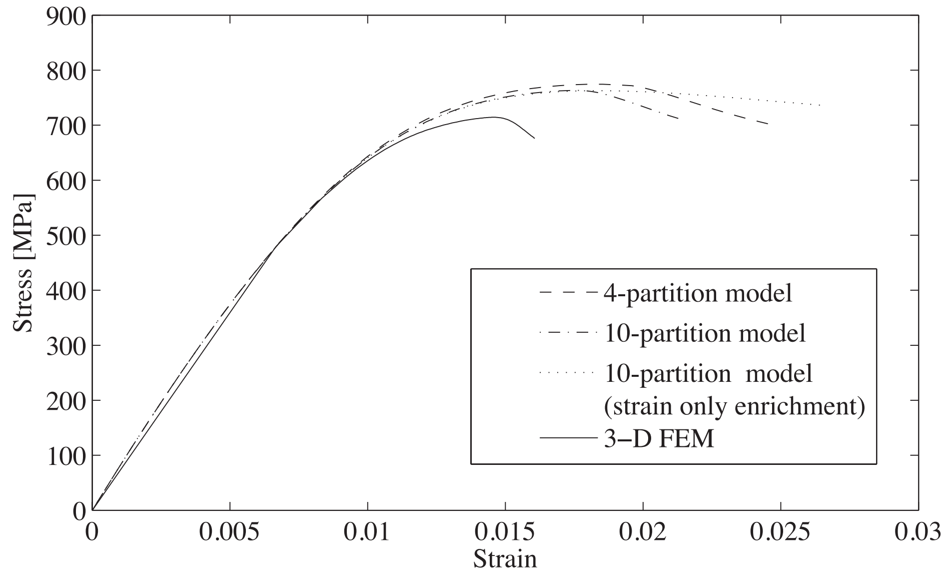

Figure 7: The stress-strain response of 4-partition and 10-partition multiscale models, strain-only enriched 10-partition model, and the reference model under uniaxial tension.

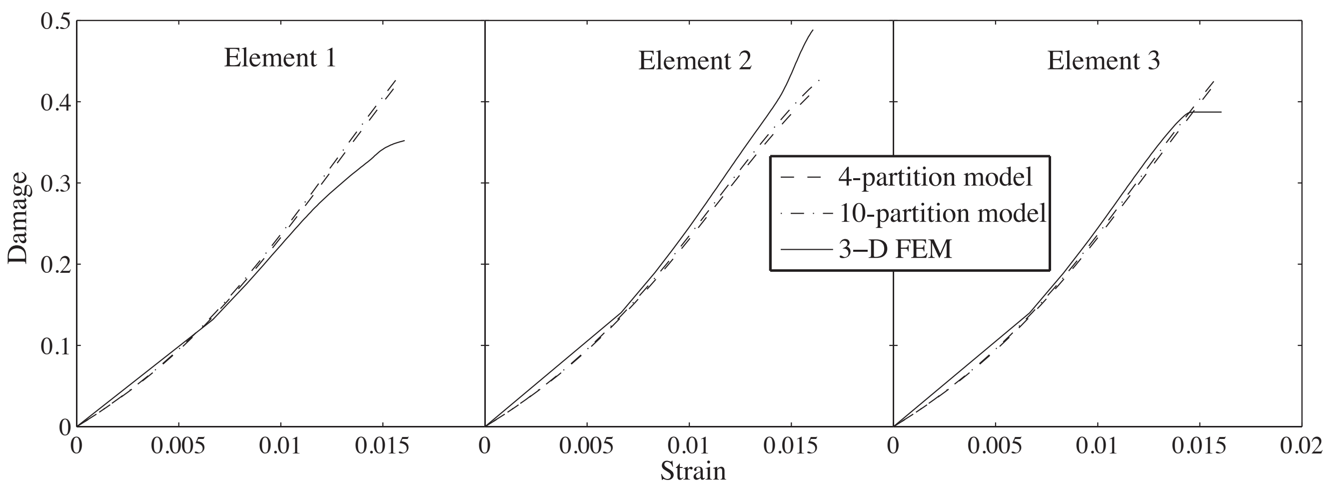

Figure 8: The average damage evolution within the matrix based on 4-partition and 10-partition multiscale models, and the reference model under uniaxial tension.

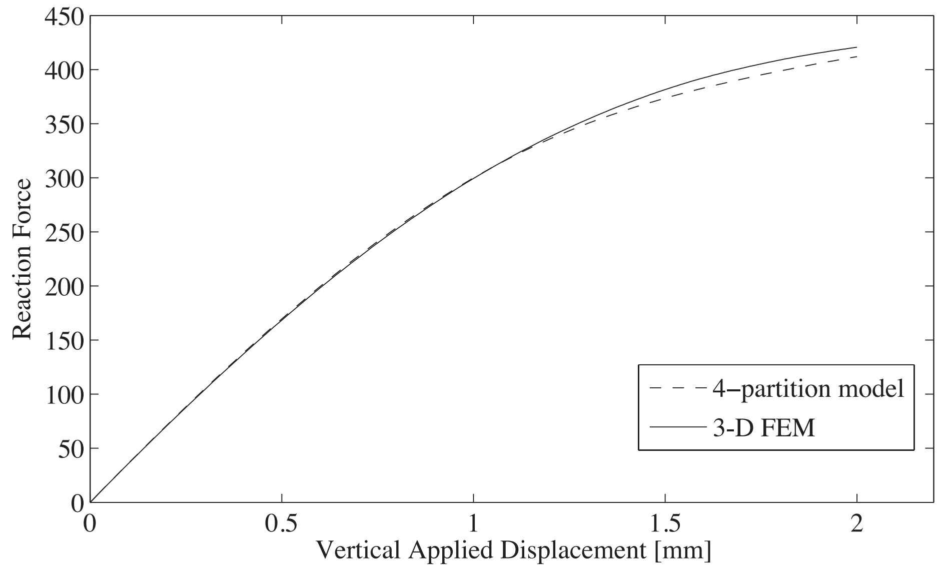

Figure 9: The reaction force-applied displacement curve of the 4-point bending plate.

the multiscale model closely matches the 3-D simulations with the lowermost layer having the higher damage accumulation rate. While the reference model predicts a periodic phase damage, the effect is smeared by the multiscale model, since the damage within each partition shown in Fig 10 is assumed to be uniform.

4.5.3 Failure of a Cracked Plate under Tension

The performance of the proposed multiscale approach is further verified by analyzing cracked composite plate subjected to tension. A quarter of the plate structure is illustrated in Fig. 11. The plate consists of a two-layer woven composite system. The geometry of the microstructure is identical to the linear plate explained in Section 3.4. The length of the center crack is 1/4 of the width of the plate. The plate is subjected to uniaxial tension perpendicular to the crack direction until failure.

The material parameters employed in the simulations for the interphase, matrix and fiber tows are summarized in Table 4. The composite plate is assumed to fail by matrix cracking and fiber breakage. The reference solution is provided by three-dimensional finite element analysis with full resolution of the microstructure throughout the plate. The discretization of the three-dimensional reference model is shown in Fig. 11. 7-partition multiscale model is employed to verify the proposed multiscale methodology. In the 7-partition model, the matrix within each layer, the interphase, 0- and 90- direction fibers in each layer constitute separate phases. The macroscopic plate is discretized using 8-node quadrilateral plate elements enriched by the multiscale enrichment functions.

The constitutive response of the woven composite plate as predicted by the proposed multiscale model and the reference model is illustrated in Fig. 12. The fracture stress and strain is predicted to be (145.7MPa, 0.464%) and (130.7MPa, 0.51%) by the multiscale and reference models, respectively. The modeling errors introduced by the plate theory and the reduction methodology amounts to 11.5% and 9% for the fracture stress and strains, respectively. The damage profiles of the composite microconstituents, including average damage in the matrix, interphase and fibers in 0- and 90- directions for top and bottom layers, are shown in Fig. 13.

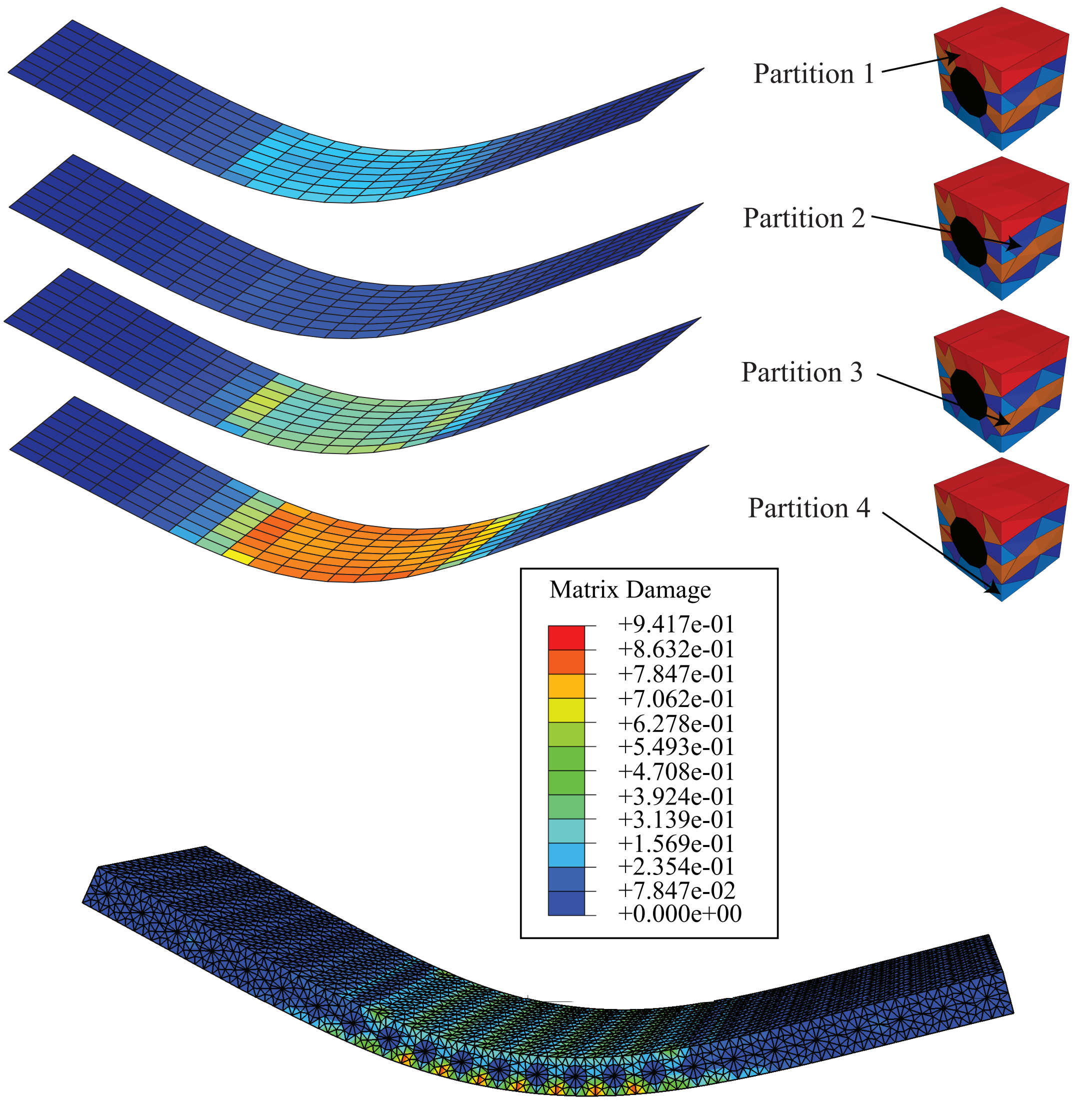

Figure 10: The damage profiles for the 4-point bending plate.

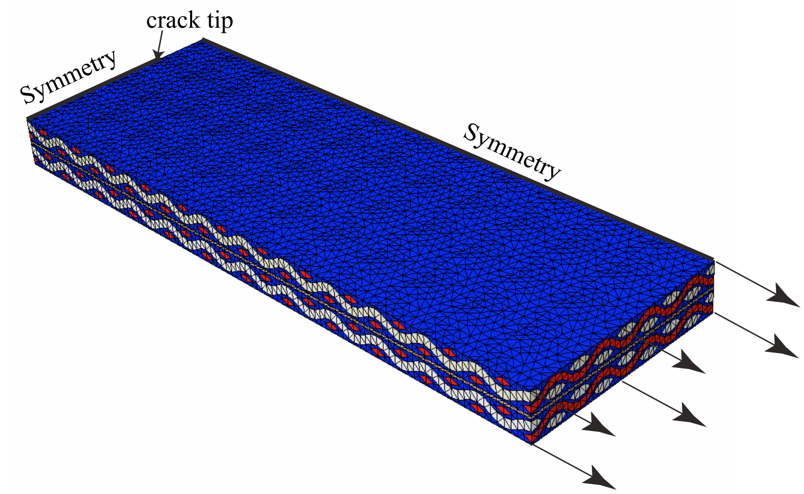

Figure 11: The geometry of the woven-composite plate with a center crack under tensile loading. Quarter of the plate is modeled due to symmety.

Table 4: Material property values for the microconstituents in the woven composite plate.

Constituent	$E[GPa]$	ν	a_1^{ph}	a_2^{ph}	c_1	c_2	υ_{ini}
Matrix	3.0	0.35	16.0	0.5	1e5	0.0	0.0
Interphase	3.0	0.35	16.0	0.5	1e5	0.0	0.0
Fiber	60.0	0.35	0.7	1.0	1e5	0.0	0.0

The failure response of the multiscale model is in reasonable agreement with the reference 3-D finite element simulations.

5 Conclusions

In this manuscript, a two-level enrichment strategy for analysis of linear and nonlinear heterogeneous plates is presented. The enrichment strategy consists of a strain-level enrichment using the mathematical homogenization theory, and a displacement-level enrichment using the partition of unity. Both the displacements and the strains are enriched using linear and nonlinear influence functions of the computational homogenization theory.

The proposed multiscale enrichment strategy is verified against direct three-dimensional finite element simulations, in which, the microscale is explicitly resolved throughout the macroscopic plate domain. The numerical simulations demonstrated that the linear and failure response of thin heterogeneous structures are predicted by good accuracy and computational efficiency. The reduction in the computational cost is due to (1) the novel integration scheme for multiscale enrichment, which eliminates the requirement for homogenization-like integration scheme, and (2) the eigendeformation-based model reduction methodology in evaluation of the nonlinear response.

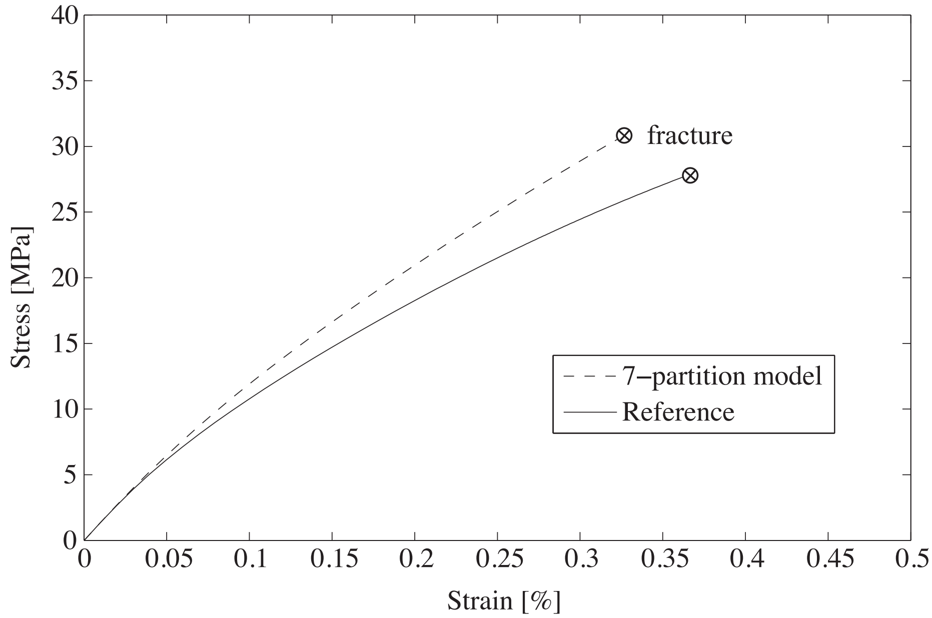

Figure 12: Comparison of the stress-strain response of cracked woven composite plate computed by the reference and multiscale models.

A Properties of the Elastic Influence Functions:

We illustrate the properties of the elastic influence functions using a homogeneous RVE (i.e., $L_{ijkl}(\mathbf{x}) = L_{ijkl}$). When a homogeneous RVE is considered, the equilibrium equation of the IFP1 reduces to:

$$L_{ijmn} H^{1}_{(m,n)kl,j} = 0 \tag{73}$$

When considering the fully periodic boundary conditions for three-dimensional homogenization problem, the constant strain modes are eliminated, leading to a trivial solution of this problem. The boundary conditions of the IFP1 problem permit constant strain modes along the thickness direction. Hence the solution of the problem above is not trivial. Equation 77 is satisfied for a constant strain field with nonzero components $H_{(3,3)kl}$. The elastic influence function is obtained by using the traction free boundary conditions:

$$n_i L_{ijmn} \left(H^{1}_{(m,n)kl} + I_{mnkl} \right) n_j = 0 \text{ on } \partial \mathcal{Y}^{\mathrm{z}} \tag{74}$$

Considering an isotropic material with normal coincident with $\mathbf{e}_3$, the nonzero components of the elastic influence function are obtained as:

$$H^{1}_{311} = H^{1}_{322} = -\frac{\lambda z}{\lambda + 2\mu}; \quad H^{1}_{333} = -z \tag{75}$$

It is worth noting that the homogenized tensor of elastic moduli, $\bar{L}_{ijkl}$, with the boundary conditions above reduces to the plane-stress tensor of elastic moduli:

$$\bar{L}_{ijmn} := \left\langle L_{ijkl} \left(H^{1}_{(k,l)mn} + I_{klmn} \right) \right\rangle = \bar{\lambda} \delta_{ij} \delta_{mn} + 2\mu I_{ijmn} \tag{76}$$

where, $\bar{\lambda} = 2\lambda\mu/(\lambda + 2\mu)$. The RVE average of the first order elastic influence function vanish: $\left\langle H^{1}_{ikl} \right\rangle = 0$.

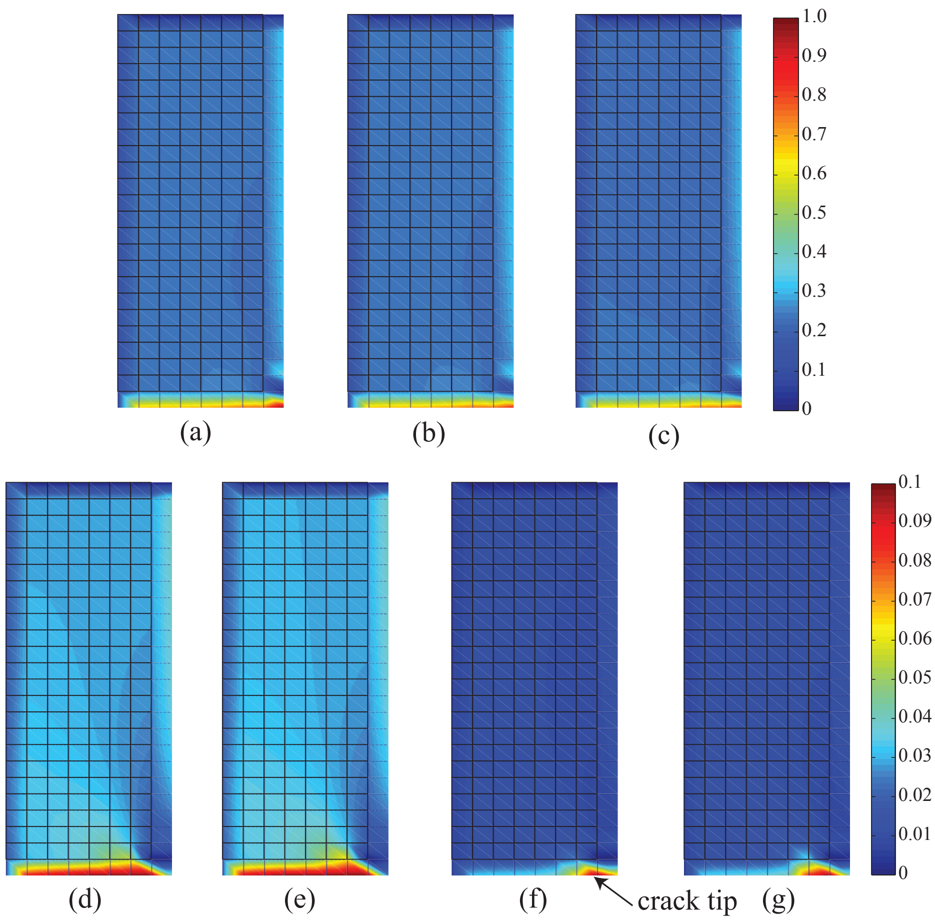

Figure 13: Damage profiles predicted by the proposed multiscale model: (a) top layer matrix phase; (b) bottom layer matrix phase; (c) interphase; (d) top layer 90-direction fiber phase; (e) bottom layer 90-direction fiber phase; (f) top layer 0-direction fiber phase; (g) bottom layer 0-direction fiber phase.

Consider the IFP2 problem on a homogeneous RVE. The equilibrium equation becomes:

$$L_{ijmn}H^1_{(m,n)kl,j} - L_{i3kl} = 0 \tag{77}$$

The solution of the IFP2 problem may be obtained by employing the traction free boundary conditions of the RVE problem. In an isotropic material, the second order elastic influence function is of the following quadratic form:

$$H^2_{311} = H^2_{322} = \frac{\lambda}{2(\lambda+2\mu)}\left(\frac{t^2}{4} - z^2\right) \tag{78}$$

$$H^2_{333} = H^2_{113} = H^2_{223} = \frac{1}{2}\left(\frac{t^2}{4} - z^2\right) \tag{79}$$

The remaining components of H^2_{ikl} are zero. It is worth noting that in contrast to the second order influence function with periodic boundary conditions, the RVE average of the second order influence function is nonzero: $\langle H^2_{ikl}\rangle \neq 0$.

B Derivation of the Hill-Mandel Energy Condition

In this section, the Hill-Mandel Energy condition (Eq. 23) is derived. We start by the expansion of the average energy term within a unit cell:

$$\begin{aligned}
\langle \sigma_{ij}\epsilon_{ij}\rangle = {} & e_{\gamma\eta}\left[\left\langle A^1_{ij\gamma\eta}L_{ijkl}A^1_{kl\alpha\beta}\right\rangle e_{\alpha\beta} + \left\langle A^1_{ij\gamma\eta}L_{ijkl}A^2_{kl\alpha\beta}\right\rangle \kappa_{\alpha\beta} + \left\langle A^1_{ij\gamma\eta}L_{ijkl}A^3_{kl\alpha}\right\rangle \gamma_\alpha\right.\\
& \left.+ \left\langle A^1_{ij\gamma\eta}L_{ijkl}G_{klA}\right\rangle \eta_A + \left\langle A^1_{ij\gamma\eta}L_{ijkl}H_{kA}\right\rangle \eta_{A,l}\right] + \kappa_{\gamma\eta}\left[\left\langle A^2_{ij\gamma\eta}L_{ijkl}A^1_{kl\alpha\beta}\right\rangle e_{\alpha\beta}\right.\\
& + \left\langle A^2_{ij\gamma\eta}L_{ijkl}A^2_{kl\alpha\beta}\right\rangle \kappa_{\alpha\beta} + \left\langle A^2_{ij\gamma\eta}L_{ijkl}A^3_{kl\alpha}\right\rangle \gamma_\alpha + \left\langle A^2_{ij\gamma\eta}L_{ijkl}G_{klA}\right\rangle \eta_A\\
& \left.+ \left\langle A^1_{ij\gamma\eta}L_{ijkl}H_{kA}\right\rangle \eta_{A,l}\right] + \gamma_\eta\left[\left\langle A^3_{ij\eta}L_{ijkl}A^1_{kl\alpha\beta}\right\rangle e_{\alpha\beta} + \left\langle A^3_{ij\eta}L_{ijkl}A^2_{kl\alpha\beta}\right\rangle \kappa_{\alpha\beta}\right.\\
& \left.+ \left\langle A^3_{ij\eta}L_{ijkl}A^3_{kl\alpha}\right\rangle \gamma_\alpha + \left\langle A^3_{ij\eta}L_{ijkl}G_{klA}\right\rangle \eta_A + \left\langle A^3_{ij\eta}L_{ijkl}H_{kA}\right\rangle \eta_{A,l}\right]\\
& + \eta_B\left[\left\langle G_{ijB}L_{ijkl}A^1_{kl\alpha\beta}\right\rangle e_{\alpha\beta} + \left\langle G_{ijB}L_{ijkl}A^2_{kl\alpha\beta}\right\rangle \kappa_{\alpha\beta} + \left\langle G_{ijB}L_{ijkl}A^3_{kl\alpha}\right\rangle \gamma_\alpha\right.\\
& \left.+ \langle G_{ijB}L_{ijkl}G_{klA}\rangle \eta_A + \langle G_{ijB}L_{ijkl}H_{kA}\rangle \eta_{A,l}\right] + \eta_{B,j}\left[\left\langle H_{iB}L_{ijkl}A^1_{kl\alpha\beta}\right\rangle e_{\alpha\beta}\right.\\
& + \left\langle H_{iB}L_{ijkl}A^2_{kl\alpha\beta}\right\rangle \kappa_{\alpha\beta} + \left\langle H_{iB}L_{ijkl}A^3_{kl\alpha}\right\rangle \gamma_\alpha + \langle H_{iB}L_{ijkl}G_{klA}\rangle \eta_A\\
& \left.+ \langle H_{iB}L_{ijkl}H_{kA}\rangle \eta_{A,l}\right]
\end{aligned} \tag{80}$$

Minor symmetry of L_{ijkl} is employed to obtain the expansion above. We will show that the following expressions hold:

$$\left\langle A^1_{ij\gamma\eta}L_{ijkl}A^p_{kl\alpha\beta}\right\rangle = \left\langle L_{\gamma\eta kl} : A^p_{kl\alpha\beta}\right\rangle; \quad \left\langle A^1_{ij\gamma\eta}L_{ijkl}A^3_{kl\alpha}\right\rangle = \left\langle L_{\gamma\eta kl} : A^3_{kl\alpha}\right\rangle \tag{81a}$$

$$\left\langle A^3_{ij\eta}L_{ijkl}A^p_{kl\alpha\beta}\right\rangle = \left\langle L_{3\eta kl} : A^p_{kl\alpha\beta}\right\rangle; \quad \left\langle A^3_{ij\eta}L_{ijkl}A^3_{kl\alpha}\right\rangle = \left\langle L_{3\eta kl} : A^3_{kl\alpha}\right\rangle \tag{81b}$$

$$\left\langle A^2_{ij\gamma\eta}L_{ijkl}A^p_{kl\alpha\beta}\right\rangle = -\left\langle zL_{\gamma\eta kl} : A^p_{kl\alpha\beta}\right\rangle; \quad \left\langle A^2_{ij\gamma\eta}L_{ijkl}A^3_{kl\alpha}\right\rangle = -\left\langle zL_{\gamma\eta kl} : A^3_{kl\alpha}\right\rangle \tag{81c}$$

where $p = 1, 2$. First, we show that Eq. 81a holds. Exploiting the definition of $A^1_{ij\gamma\eta}$, Eq. 81a can be written as:

$$\left\langle A^1_{ij\gamma\eta}L_{ijkl}A^p_{kl\alpha\beta}\right\rangle = \left\langle L_{\gamma\eta kl}A^p_{kl\alpha\beta}\right\rangle + \left\langle G^1_{ij\gamma\eta}L_{ijkl}A^p_{kl\alpha\beta}\right\rangle \tag{82}$$

Applying the chain rule and the Green's theorem, the second term yields:

$$\left\langle G^1_{ij\gamma\eta} L_{ijkl} A^p_{kl\alpha\beta} \right\rangle =$$
$$\frac{1}{|\mathcal{Y}|}\left[\int\limits_{\partial\mathcal{Y}^{\rm per}} H^1_{i\gamma\eta} L_{ijkl} A^p_{kl\alpha\beta} n_j d\Gamma + \int\limits_{\partial\mathcal{Y}^{\rm z}} H^1_{i\gamma\eta} L_{ijkl} A^p_{kl\alpha\beta} n_j d\Gamma + \int\limits_{\mathcal{Y}} H^1_{i\gamma\eta}\left(L_{ijkl} A^p_{kl\alpha\beta}\right)_{,j} d\mathcal{Y}\right] \tag{83}$$

Using the definitions of the IFP1 and IFP2 problems, we observe that all terms vanish in the equation above (first by periodicity, second by periodicity and zero traction condition and third by equilibrium). By this results, the coupling terms between η_A, and the in-plane strain, curvature and transverse shear strains vanish (i.e., $\left\langle G_{ijB} L_{ijkl} A^1_{kl\alpha\beta}\right\rangle = \left\langle G_{ijB} L_{ijkl} A^2_{kl\alpha\beta}\right\rangle = 0$ and $\langle G_{ijB} L_{ijkl} A^3_{kl\alpha}\rangle = 0$). The derivation of the second part of Eq. 81a as well as Eq. 81b follows the ideas above and skipped in this presentation.

Equation 81c is shown to hold by exploiting the definition of $A^2_{ij\gamma\eta}$:

$$\left\langle A^2_{ij\gamma\eta} L_{ijkl} A^p_{kl\alpha\beta}\right\rangle = \left\langle -z L_{\gamma\eta kl} A^p_{kl\alpha\beta}\right\rangle + \left\langle G^2_{ij\gamma\eta} L_{ijkl} A^p_{kl\alpha\beta}\right\rangle \tag{84}$$

and observing that the second term vanishes by the same arguments applied to the second term of Eq. 82. Equation 24 is achieved by denoting the nonzero components in Eq. 80 as in Eq. 26. In the absence of the displacement level enrichment, the energy conjugate of the in-plane strains, curvature and transverse shear strains are the homogenized in-plane force, moment and shear force resultants, respectively. In the presence of displacement level enrichment, the generalized stress tensors do not yield the same physical meaning despite being the energy conjugates of the corresponding strain measures. The in-plane force resultants, bending and shear forces are calculated by appropriate averaging over the RVE.

C Acknowledgements

The faculty start-up funds provided by Vanderbilt University are gratefully acknowledged.

References

[1] I. Babuska. Homogenization and application. mathematical and computational problems. In B. Hubbard, editor, *Numerical Solution of Partial Differential Equations - III, SYNSPADE.* Academic Press, 1975.

[2] A. Bensoussan, J. L. Lions, and G. Papanicolaou. *Asymptotic Analysis for Periodic Structures.* North-Holland, Amsterdam, 1978.

[3] E. Sanchez-Palencia. *Non-homogeneous media and vibration theory*, volume 127 of *Lecture notes in physics.* Springer-Verlag, Berlin, 1980.

[4] P. M. Suquet. Elements of homogenization for inelastic solid mechanics. In E. Sanchez-Palencia and A. Zaoui, editors, *Homogenization Techniques for Composite Media.* Springer-Verlag, 1987.

[5] Z. Yuan and J. Fish. Towards realization of computational homogenization in practice. *Int. J. Numer. Meth. Engng.*, 73:361–380, 2008.

[6] T. J. R. Hughes. Multiscale phenomena: Green's functions, the dirichlet-to-neumann formulation, subgrid-scale models, bubbles and the origins of stabilized methods. *Comp. Meth. Appl. Mech. Engng.*, 127:387–401, 1995.

[7] I. Babuska and J. Melenk. The partition of unity method. *Int. J. Numer. Meth. Engng.*, 40:727–758, 1997.

[8] T. Tang and W. Yu. Variational asymptotic homogenization of heterogeneous electromagnetoelastic materials. *International Journal of Engineering Science*, 46(8):741–757, AUG 2008.

[9] W. B. Yu. Mathematical construction of a reissner-mindlin plate theory for composite laminates. *International Journal of Solids and Structures*, 42(26):6680–6699, DEC 2005.

[10] W. Yu and T. Tang. A variational asymptotic micromechanics model for predicting thermoelastic properties of heterogeneous materials. *Int. J. Solids Struct.*, 44:7510–7525, 2007.

[11] J. T. Oden and T. I. Zohdi. Analysis and adaptive modeling of highly heterogeneous elastic structures. *Comput. Methods. Appl. Mech. Engng.*, 148:367–391, 1997.

[12] J. Fish and Z. Yuan. Multiscale enrichment based on partition of unity. *Int. J. Numer. Meth. Engng.*, 62:1341–1359, 2005.

[13] J. Fish and Z. Yuan. Multiscale enrichment based on partition of unity for nonperiodic fields and nonlinear problems. *Comp. Mech.*, 40:249–259, 2007.

[14] F. Feyel and J.-L. Chaboche. Fe2 multiscale approach for modelling the elastoviscoplastic behavior of long fiber sic/ti composite materials. *Comput. Methods Appl. Mech. Engrg.*, 183:309–330, 2000.

[15] S. Ghosh and S. Moorthy. Elastic-plastic analysis of arbitrary heterogeneous materials with the voronoi cell finite element method. *Comput. Methods Appl. Mech. Engng.*, 121(1-4):373–409, 1995.

[16] H. Moulinec and P. Suquet. A numerical method for computing the overall response of nonlinear composites with complex microstructure. *Comput. Meth. Appl. Mech. Engng*, 157:69–94, 1998.

[17] J. Aboudi. A continuum theory for fiber-reinforced elastic-viscoplastic composites. *J. Eng. Sci.*, 20(55):605–621, 1982.

[18] J. Yvonnet and Q. C. He. The reduced model multiscale method (R3M) for the non-linear homogenization of hyperelastic media at finite strains. *J. Comput. Physics*, 223:341–368, 2007.

[19] J. Fish, Q. Yu, and K. L. Shek. Computational damage mechanics for composite materials based on mathematical homogenization. *Int. J. Numer. Meth. Engng.*, 45:1657–1679, 1999.

[20] J. L. Chaboche, S. Kruch, J. F. Maire, and T. Pottier. Towards a micromechanics based inelastic and damage modeling of composites. *Int. J. Plasticity*, 17:411–439, 2001.

[21] J. C. Michel and P. Suquet. Nonuniform transformation field analysis. *Int. J. Solids Structures*, 40:6937–6955, 2003.

[22] Y. A. Bahei-El-Din, A. M. Rajendran, and M. A. Zikry. A micromechanical model for damage progression in woven composite systems. *Int. J. Solids Structures*, 41:2307–2330, 2004.

[23] C. Oskay and J. Fish. Eigendeformation-based reduced order homogenization for failure analysis of heterogeneous materials. *Comp. Meth. Appl. Mech. Engng.*, 196(7):1216–1243, 2007.

[24] D Caillerie. Thin elastic and periodic plates. *Math. Meth. Appl. Sci.*, 6:159–191, 1984.

[25] D Cioranescu and J. Saint Jean Paulin. *Homogenization of Reticulated Structures.* Springer, Berlin, 1999.

[26] R.V. Kohn and M. Vogelius. A new model for thin plates with rapidly varying thickness. *Int. J. Solids Struct.*, 20:333–350, 1984.

[27] A. G. Kolpakov. Calculation of the characteristics of thin elastic rods with a periodic structure. *Pmm Journal of Applied Mathematics and Mechanics*, 55:358–365, 1991.

[28] L. Trabucho and J. M. Viano. Mathematical modeling of rods. In P.G. Ciarlet and J. L. Lions, editors, *Handbook of Numerical Analysis*, volume IV. Elsevier, 1996.

[29] N. Buannic and P. Cartraud. Etude comparative de methodes d'homogeneisation pour des structures periodiques elancees. In *Proceedings of the 14eme Congres Francais de Mecanique*, Toulouse, France, 1999.

[30] C. Oskay and G. Pal. A multiscale failure model for analysis of thin heterogeneous plates. *Int. J. Damage Mechanics*, 2008 (in review).

[31] J. N. Reddy. *Mechanics of Laminated Composite Plates and Shells: Theory and Analysis.* CRC Press, second edition, 1997.

[32] T. J. R. Hughes. *The Finite Element Method.* Dover Publications, 2003.